European Journal of Mechanics / A Solids 108 (2024) 105410

Contents lists available at ScienceDirect

European Journal of Mechanics / A Solids

journal homepage: www.elsevier.com/locate/ejmsol

Full length article

Macroscopic modeling of flexoelectricity-driven remanent polarization in piezoceramics

Felix Sutter *, Marc Kamlah

Institute for Applied Materials, Karlsruhe Institute of Technology (KIT), Hermann-von-Helmholtz-Platz 1, 76344 Eggenstein-Leopoldshafen, Germany

ARTICLE INFO

Keywords:
Flexoelectricity
Ferroelectricity
Piezoceramics
Variational modeling framework
Macroscopic non-linear model
Mixed finite elements

ABSTRACT

This paper presents a variational modeling framework for investigating the flexoelectricity-driven evolution of remanent polarization in piezoceramics. In small-scale electromechanical systems, strain gradients can exhibit polarization in dielectric materials via the direct flexoelectric effect. In ferroelectrics, it is reasonable to expect that a sufficiently large magnitude of the flexoelectricity leads to a switching of the domain structure and thus the material becomes remanently polarized. It is interesting to note that this means that poling would be able to occur in the absence of any external electrical source. This provides the motivation to gain a better understanding of this effect for a possible technical use in e.g. sensor applications. For this purpose, a macroscopic model is presented that couples flexoelectricity and ferroelectric domain switching processes. By embedding the model in the variational framework of the generalized standard materials (GSM), a minimum-type potential structure and thus a stable and efficient numerical treatment is obtained. A mixed finite element formulation based on the Helmholtz free energy is introduced to solve the higher-order flexoelectric boundary value problem. In order to realistically predict the flexoelectric material behavior, the model response is adapted to experimental results in literature obtained for a piezoceramic in a bending test. By simulations based on the adapted model the evolution of the flexoelectricity-driven remanent polarization in the vicinity of a notch is shown.

1. Introduction

Currently, there is a trend towards miniaturization of micro-electro-mechanical systems (MEMS) in the field of sensing and actuation. As the component dimension decreases, size-dependent material properties become increasingly influential in the material behavior. Therefore, it is worth considering the size-dependent effect of flexoelectricity, which has received significant attention in the scientific community, cf. e.g. Yudin and Tagantsev (2013), Zubko et al. (2013), Wang et al. (2019) and Shu et al. (2019). In general, the direct flexoelectric effect refers to the electromechanical coupling between the mechanical strain gradient and the electric polarization in a dielectric, occurring independently of its crystal symmetry.

In ferroelectric ceramics, such as lead zirconate titanate (PZT) or barium titanate ($BaTiO_3$), significant manifestations of flexoelectric coupling properties have been observed (Ma and Cross, 2005; Wang et al., 2013; Ma and Cross, 2006). In addition, they possess pronounced piezoelectric properties, making them a popular choice for sensing and actuation applications. To activate these piezoelectric coupling properties in a ferroelectric polycrystal, a poling process has to be performed under the action of high electric fields. During this process, at the microstructural level, the initially randomly oriented domains undergo irreversible alignment in the direction of the applied field. This results in a highly non-linear material behavior, which includes a significant increase of the macroscopic polarization and strain with an irreversible character. Under cyclic conditions, the characteristic large signal hysteresis phenomena of ferroelectrics can be observed, cf. e.g. Jaffe et al. (1971) and Moulson and Herbert (2003). Multiaxial phenomenological constitutive models for the hysteretic behavior of ferroelectrics are given e.g. in Kamlah and Böhle (2001), Landis (2002), Kamlah and Wang (2003) and Mehling et al. (2007), see also (Kamlah, 2001; Landis, 2004; Sutter and Kamlah, 2023) and the references therein.

The direct flexoelectric effect can be interpreted as an internal electric driving force generated by an inhomogeneous deformation. This motivates the idea of initiating poling processes in ferroelectrics using this effect without the need for an external electrical source. It has already been experimentally demonstrated that a local external mechanical load can affect the domain state in the material and create

* Corresponding author.
E-mail addresses: felix.sutter@kit.edu (F. Sutter), marc.kamlah@kit.edu (M. Kamlah).

https://doi.org/10.1016/j.euromechsol.2024.105410
Received 24 April 2024; Received in revised form 28 June 2024; Accepted 26 July 2024
Available online 29 July 2024

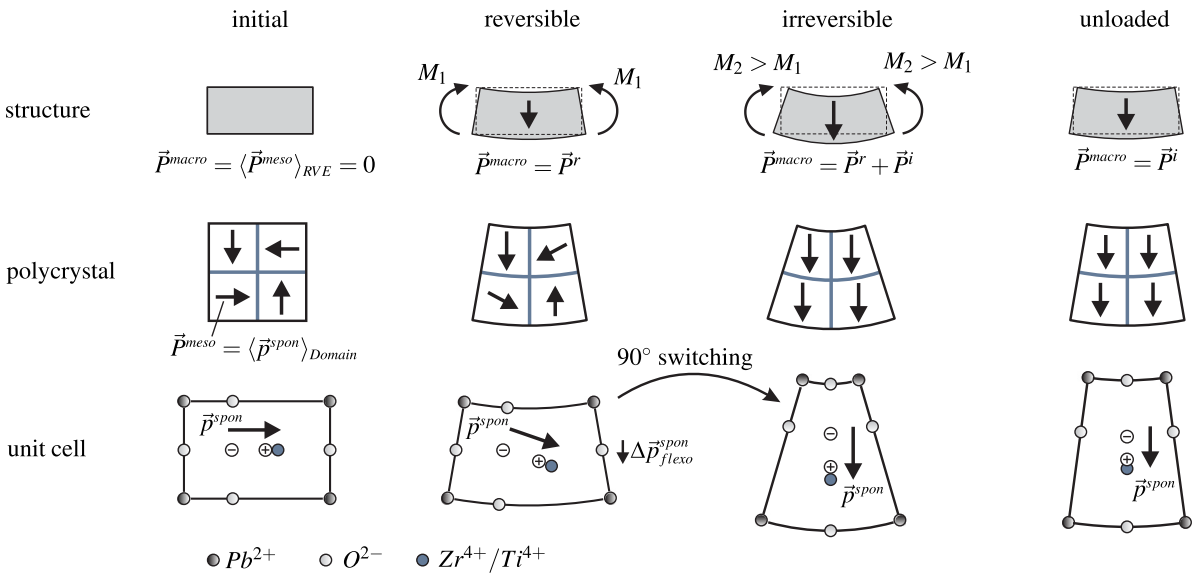

Fig. 1. Consideration of the mechanisms underlying the formation of remanent polarization in ferroelectric materials (e.g. PZT) driven by flexoelectricity.

a remanent polarization (Bursian et al., 1969; Gruverman et al., 2003; Lu et al., 2012). However, quantifying the contribution of flexoelectricity to domain switching processes is challenging due to the complex loading states required to generate strain gradients in the material. Therefore, simulations are necessary to gain a deeper understanding of the underlying mechanisms and to maintain the perspective of being able to use the effect specifically in technical applications.

Numerical studies of the domain switching behavior in ferroelectrics, including flexoelectricity, have been performed using phase field methods, cf. e.g. Liu et al. (2019), Cao et al. (2006), Chen et al. (2014), Gu et al. (2015), Jiang et al. (2015b,a), Cao et al. (2015) and Cao et al. (2017). However, due to the high computational demand, only a few domains in a single crystal are typically taken into account, which makes the consideration of entire components questionable. On a macroscopic continuum scale, flexoelectric models are often based on the strain gradient theory formulated by Mindlin and Eshel (1968). The resulting boundary value problems arise as fourth-order partial differential equations, which cannot be solved using conventional finite element approaches. Therefore, various alternative numerical methods are used in the literature, like e.g. isogeometric methods (Ghasemi et al., 2017; Thai et al., 2018; Nguyen et al., 2018, 2019), meshless methods (Abdollahi et al., 2014; Zhuang et al., 2020a), mixed finite element methods (Deng et al., 2017; Mao et al., 2016; Serrao and Kozinov, 2023), collocation mixed finite element methods (Tian et al., 2021; Tannhäuser et al., 2023, 2024), C0 interior penalty FE methods (Ventura et al., 2021; Balcells-Quintana et al., 2022), immersed boundary methods (Codony et al., 2019) and peridynamics (Roy and Roy, 2019). For a detailed review of computational modeling of flexoelectricity, see Zhuang et al. (2020b) and Codony et al. (2021b).

Most numerical studies on flexoelectricity in ferroelectrics at the macroscopic scale have been conducted under the assumption of linear material behavior, e.g. Abdollahi et al. (2014) and Nguyen et al. (2018). Material non-linearities are considered in the continuum modeling of flexoelectricity, for example, in the form of hyperelasticity in Yvonnet and Nguyen (2017), Thai et al. (2018), Nguyen et al. (2019), Codony et al. (2021a) and Deng et al. (2023) or viscoelasticity in Sladek et al. (2022). In Witt et al. (2023, 2024), dissipative effects of irreversible character were considered in a coupling with diffusion problems to simulate the healing of microcracks in human bone. Recently, Serrao and Kozinov (2024) presented a model that takes into account the flexoelectricity in ferroelectric solids, including domain switching effects in a micromechanical framework. The numerical investigations carried out there provide interesting insights into the influence of the converse flexoelectric effect on the dielectric hysteresis and the butterfly hysteresis.

The objective of the present work is, first, to introduce a variational flexoelectric continuum modeling framework capable of describing the dissipative domain switching processes in ferroelectrics under quasi-static conditions and, second, to investigate the effect of direct flexoelectricity on the evolution of remanent polarization. This provides a perspective to gain a deeper understanding of the interplay of flexoelectricity and poling-induced piezoelectricity in ferroelectric engineering devices. Therefore, it is possible to examine the potential for purely mechanically induced poling processes in ferroelectrics. For this purpose, the minimum-type variational modeling framework introduced in Sutter and Kamlah (2023) is extended to include the flexoelectric effect, and a suitable mixed finite element formulation is presented for solving the higher-order global boundary value problems. Essential aspects of the presented numerical investigations are, on the one hand, a comparison with experimental results on the macroscopic flexoelectric response of real piezoceramics and parameter fitting. On the other hand, unloaded states are considered where remanent effects on the polarization state due to the flexoelectric effect become clearly visible.

2. Preliminary scale-bridging considerations for the evolution of flexoelectricity-driven remanent polarization

In a first step, we want to give a – from the authors point of view – plausible interpretation of purely flexoelectricity-driven remanent polarization appearing on the macroscopic continuum scale in ferroelectric polycrystals. In these considerations we will also take into account the mesoscopic domain structure of the polycrystal as well as the unit cell level, cf. Fig. 1.

Consider a beam-like structure made of ferroelectric material in an initial thermally depolarized state. A unit cell of its crystal lattice has an asymmetric tetragonal configuration with a microscopic dipole resulting in a spontaneous polarization. The polycrystalline structure consists of grains where each grain contains domains of a homogeneous crystal lattice with coaxially oriented spontaneous polarization vectors of all unit cells. The averaged polarization for a representative volume element (RVE) – with a sufficient number of grains – of such

a material would vanish due to the random distribution of the domain orientations.

An applied bending moment would cause a strain gradient in the structure, which would also be noticeable at the level of the unit cells. The non-symmetric deformation of the cell causes a charge redistribution and thus forms an additional spontaneous polarization component that can be attributed to the flexoelectric effect. This flexoelectric polarization is superimposed on all unit cells of a polycrystal and can therefore be measured on a macroscopic scale. If the external load does not exceed a critical value, the superimposed polarization of the material would disappear after unloading.

Now we want to consider a situation where the applied bending moment causes a strain gradient of high magnitude. The atomistic flexoelectric effect would then lead to a redistribution of the ions appearing as 90° or 180° ferroelectric switching of a unit cell. This switching process takes place in all domains of the polycrystal under the action of a sufficiently large strain gradient and leads to a macroscopic polarization of the material. The remanent characteristic of this polarization becomes visible after unloading. Other than the vanishing reversible polarization $\vec{P}^r$ an irreversible polarization $\vec{P}^i$ remains in the sample. Therefore, the material exhibits a poling process under mechanical loading driven by the flexoelectric effect, without any electrical stimulus.

In this simplified illustration of the emergence of a remanent polarization in ferroelectrics caused by flexoelectricity, we have initially neglected the occurrence of ferroelastic domain switching processes for the sake of clarity. In the numerical examples discussed in this paper, we will see that they play an important role. Their occurrence becomes visible in a permanent deformation of the unloaded sample, as indicated in Fig. 1.

3. Flexoelectric field theory for ferroelectric materials

In this section, the field quantities of an electro-mechanically coupled continuum theory with linearized kinematics for a body $\mathcal{B}$ are introduced. This theory takes into account flexoelectricity as well as dissipative effects caused by ferroelectric or ferroelastic domain switching mechanisms in the material. Only quasi-static loading scenarios with vanishing inertia effects are assumed. The ferroelectric materials under consideration are idealized to be non-conductive with no available free body charges and no magnetic effects. Furthermore, a constant temperature of uniform distribution is assumed for all considered processes.

3.1. Field variables

The second-order infinitesimal strain tensor

$$\boldsymbol{\varepsilon} = \frac{1}{2}(\boldsymbol{H}^T + \boldsymbol{H}) \qquad \text{or} \qquad \varepsilon_{ij} = \frac{1}{2}(u_{j,i} + u_{i,j})\,, \tag{1}$$

calculated from the displacement field $\vec{u}$ of a material point $\vec{x} \in \mathcal{B}$ via the displacement gradient $\boldsymbol{H} = \vec{u} \otimes \vec{\nabla}$, is considered as the first kinematic variable. In order to be able to describe the flexoelectric effect, a kinematic field variable of higher order must be included in the theory. For this purpose, the third-order strain gradient tensor

$$\begin{aligned} \boldsymbol{\eta} \quad &= \boldsymbol{\varepsilon} \otimes \vec{\nabla} = \frac{1}{2}\left(\boldsymbol{H}^T \otimes \vec{\nabla} + \boldsymbol{H} \otimes \vec{\nabla}\right) \\ \text{or} \quad \eta_{ijk} = \varepsilon_{ij,k} \quad &= \frac{1}{2}(u_{j,ik} + u_{i,jk}) \end{aligned} \tag{2}$$

is introduced, whose symmetry condition affects the first two indices. A detailed discussion of the symmetry conditions in strain gradient theories can be found e.g. in Gusev and Lurie (2017). Graphical representations of the various components of the strain gradient tensor can be found, for example, in Sutter (2024) and Polizzotto (2016).

The electric displacement vector

$$\vec{D} = \epsilon_0 \vec{E} + \vec{P} \tag{3}$$

is used to represent the state of charge at a material point in an insulating electro-mechanical body. While $\vec{P}$ and ϵ_0 symbolize the macroscopic polarization vector and the permittivity of the vacuum in (3), respectively, for non-magnetic materials the curl-free electric field vector

$$\vec{\nabla} \times \vec{E} = \vec{0} \quad \Longleftrightarrow \quad \vec{E} = -\vec{\nabla}\phi \tag{4}$$

is given as the negative gradient of the electric potential ϕ.

In summary, a set of intensive quantities can be represented by the set

$$\mathfrak{E} := \left\{\boldsymbol{\varepsilon},\, \boldsymbol{\eta},\, \vec{D}\right\}, \tag{5}$$

while they are defined as the *independent* field variables of the constitutive model presented here.

3.2. Internal state variables

Since the theory presented should include a non-linear material behavior with dissipative effects, as is characteristic of ferroelectrics, the possibility of the occurrence of irreversible parts in some field quantities must be considered. Therefore, an additive split of the strain tensor and the electric displacement vector according to

$$\boldsymbol{\varepsilon} = \boldsymbol{\varepsilon}^r + \boldsymbol{\varepsilon}^i(\boldsymbol{A}) \qquad \text{and} \qquad \vec{D} = \vec{D}^r + \vec{P}^i(\vec{\rho})\,, \tag{6}$$

respectively, in reversible and irreversible parts is assumed, cf. Bassiouny et al. (1988) and Bassiouny and Maugin (1989). The irreversible strain tensor in $(6)_1$

$$\boldsymbol{\varepsilon}^i(\boldsymbol{A}) = \frac{3}{2}\varepsilon^{sat}\boldsymbol{A}^{Dev} \tag{7}$$

is expressed as a function of the second-order *texture tensor* $\boldsymbol{A}$ and scaled by the macroscopic saturation strain ε^{sat}. Furthermore, the irreversible polarization vector

$$\vec{P}^i(\vec{\rho}) = P^{sat}\vec{\rho} \tag{8}$$

is written in terms of the *relative polarization vector* $\vec{\rho}$ and weighted by the saturation polarization P^{sat} of a ferroelectric polycrystal.

The two microscopically motivated internal state variables, summarized by the field

$$\mathfrak{q} := \left\{\boldsymbol{A},\, \vec{\rho}\right\}, \tag{9}$$

are based on a macroscopic modeling framework initially introduced in Kamlah and Jiang (1999) and Kamlah and Wang (2003). Later, the representation chosen in this work was presented in Mehling et al. (2007), see also (Sutter and Kamlah, 2023). It is further assumed that the history of a material point, which includes all dissipative processes that have taken place, is represented by these internal variables. Their initial values, corresponding to a thermally depolarized material state, are given by $\boldsymbol{A} = 1/3\boldsymbol{I}$ and $\vec{\rho} = [000]^T$, where $\boldsymbol{I}$ represents the second-order identity tensor.

4. Variational modeling of dissipative flexoelectric solids

In order to derive a thermodynamically consistent theory for higher order dissipative solids with a variational structure, which is sufficient to satisfy the Clausius–Duhem inequality for all admissible thermodynamic processes, the presented model is formulated within the framework of the generalized standard materials (GSM) (Halphen and Nguyen, 1975). In this context, we will follow the approach for a local theory presented in Miehe et al. (2011) and Sutter and Kamlah (2023). Hence, we consider a material point element of an electro-mechanically coupled continuum whose state is completely described by the sets of independent intensive variables $\mathfrak{E}$ and the internal state variables $\mathfrak{q}$.

4.1. Formulation of an algorithmic potential

Let us assume within a time step $\Delta t = t_{n+1} - t_n$ the existence of a local rate-type potential in its algorithmic representation (cf. Simo and Honein, 1990; Ortiz and Stainier, 1999; Radovitzky and Ortiz, 1999; Miehe, 2002)

$$\pi(\mathfrak{E}, \mathfrak{q}) := \pi^{int}(\mathfrak{E}, \mathfrak{q}) - \mathcal{P}^{ext}(\mathfrak{E}) \tag{10}$$

with the internal contribution

$$\pi^{int}(\mathfrak{E}, \mathfrak{q}) := \Psi(\mathfrak{E}, \mathfrak{q}) - \Psi(\mathfrak{E}_n, \mathfrak{q}_n) + \Delta t \Phi\big(\tfrac{1}{\Delta t}(\mathfrak{q} - \mathfrak{q}_n)\big)\,, \tag{11}$$

where the quantities with the subscript $\square_n$ represent their states at time t_n, while the subscript of the current time t_{n+1} is omitted for simplicity. In this potential, the energy storage per unit volume is described by the convex Helmholtz free energy function Ψ and the energy dissipation by a convex, normalized and non-negative dissipation potential Φ. The external load function assumed to be given for time t_{n+1} is defined as

$$\mathcal{P}^{ext}(\mathfrak{E}) := \mathfrak{S} \cdot (\mathfrak{E} - \mathfrak{E}_n) \tag{12}$$

depending on the external loading

$$\mathfrak{S} := \big\{\boldsymbol{\sigma},\ \boldsymbol{\tau},\ \vec{E}\big\}\,, \tag{13}$$

with the local stress tensor $\boldsymbol{\sigma}$ of second order, the non-local stress tensor $\boldsymbol{\tau}$ of third order, the work conjugate of $\boldsymbol{\eta}$, and the electric field vector $\vec{E}$. They are called *dependent* field variables in the following.

4.2. Helmholtz free energy

For the Helmholtz free energy per unit volume the decomposition

$$\Psi(\mathfrak{E}, \mathfrak{q}) = \Psi^r(\mathfrak{E}, \mathfrak{q}) + \Psi^i(\mathfrak{q}) \tag{14}$$

in a reversible and an irreversible part is postulated, cf. Bassiouny et al. (1988). The reversible part is given by the quadratic form

$$\begin{aligned}\Psi^r(\mathfrak{E}, \mathfrak{q}) = {}& \frac{1}{2}(\boldsymbol{\varepsilon} - \boldsymbol{\varepsilon}^i) : \mathbb{C}^D : (\boldsymbol{\varepsilon} - \boldsymbol{\varepsilon}^i) + \frac{1}{2}\boldsymbol{\eta} \therefore \mathbb{G}^D \therefore \boldsymbol{\eta} \\ & + \frac{1}{2}(\vec{D} - \vec{P}^i) \cdot \boldsymbol{\beta}^{\varepsilon} \cdot (\vec{D} - \vec{P}^i) + \boldsymbol{\eta} \therefore \mathbb{b} : (\boldsymbol{\varepsilon} - \boldsymbol{\varepsilon}^i) \\ & - (\vec{D} - \vec{P}^i) \cdot \mathbb{h} : (\boldsymbol{\varepsilon} - \boldsymbol{\varepsilon}^i) - (\vec{D} - \vec{P}^i) \cdot \mathbb{f} \therefore \boldsymbol{\eta}\,,\end{aligned} \tag{15}$$

while the material tensors contained in (15) are the fourth-order elasticity tensor at constant electric displacement $\mathbb{C}^D$, the sixth-order strain gradient elasticity tensor at constant electric displacement $\mathbb{G}^D$, the second-order impermittivity tensor at constant strain $\boldsymbol{\beta}^{\varepsilon}$, the fifth-order strain coupling tensor $\mathbb{b}$, the third order piezoelectric tensor $\mathbb{h}$ and the fourth-order flexoelectric coupling tensor $\mathbb{f}$. All these tensors are functions of the relative polarization vector $\vec{\rho}$. The exact representations are derived in Appendix A. The less intuitive energy contribution from the coupling of the strain with the strain gradient in (15) is the result of a consistent derivation of the form of the Helmholtz free energy from the constitutive equations based on the electric Gibbs energy $G_2(\boldsymbol{\varepsilon}, \boldsymbol{\tau}, \vec{E})$, which is also presented in Appendix A.

The irreversible part of the Helmholtz free energy in (14) is written as

$$\begin{aligned}\Psi^i(\mathfrak{q}) = {}& \frac{1}{2}c_A \boldsymbol{A}^{Dev} : \boldsymbol{A}^{Dev} + \frac{1}{2}c_\rho \vec{\rho} \cdot \vec{\rho} \\ & + \frac{a_A}{m_A}\mathrm{tr}(\boldsymbol{A}^{-m_A}) + \frac{a_\rho}{m_\rho}(1 - \zeta)^{-m_\rho}\end{aligned} \tag{16}$$

$$\text{with} \qquad \zeta(\boldsymbol{A}, \vec{\rho}) = \|(\xi \boldsymbol{I} + (1 - \xi)\boldsymbol{A})^{-1} \cdot \vec{\rho}\|^2\,,$$

where the first two terms describe a linear kinematic hardening in the evolution of the internal state variables and the last two terms correspond to the saturation behavior characteristic for ferroelectric materials, indicating a fully oriented state of the domain structure. For more details on the different contributions in (16) see Sutter and Kamlah (2023) and Mehling et al. (2007).

4.3. Dissipation potential

In accordance with its construction in Miehe et al. (2011) and Sutter and Kamlah (2023), for a rate-independent material behavior the dissipation potential in (11) is assumed to be

$$\Phi\big(\tfrac{1}{\Delta t}(\mathfrak{q} - \mathfrak{q}_n)\big) := \sup_{\mathfrak{f}^{\mathfrak{q}}, \lambda \geq 0} \Big\{\mathfrak{f}^{\mathfrak{q}} \cdot \tfrac{1}{\Delta t}(\mathfrak{q} - \mathfrak{q}_n) - \lambda F(\mathfrak{f}^{\mathfrak{q}})\Big\}\,, \tag{17}$$

which itself appears as a maximization problem. It has to be optimized during the solution process with respect to the set of the dissipative internal driving forces

$$\mathfrak{f}^{\mathfrak{q}} := \big\{\boldsymbol{f}^A,\ \vec{f}^{\rho}\big\} \tag{18}$$

and the Lagrange multiplier λ, enforcing the fulfillment of the threshold function

$$F(\mathfrak{f}^{\mathfrak{q}}) := \frac{(\boldsymbol{f}^A)^{Dev} : (\boldsymbol{f}^A)^{Dev}}{(f_c^A)^2} + \frac{\vec{f}^{\rho} \cdot \vec{f}^{\rho}}{(f_c^{\rho})^2} - 1 \leq 0\,. \tag{19}$$

The dissipative internal forces (18) act as work conjugated quantities on the internal state variables in (9) and drive them to evolve if their magnitude leads to a violation of the threshold function (19). Physically, this process is related to the initiation of microstructural domain switching effects in real piezoceramics. The critical values in the threshold function in (19) are given by $f_c^A = \sqrt{3/2}\varepsilon^{sat}\sigma^c$ and $f_c^{\rho} = P^{sat}E^c$ with the coercive values of the stress σ^c and the electric field E^c experimentally observed for a polycrystal, cf. also Table 1.

4.4. Incremental variational principle

In order to perform an incremental constitutive update of the independent variables (5) and the internal state variables (9) of a material point within a time interval Δt based on the introduced algorithmic rate-type potential (10), the incremental variational principle

$$\big\{\mathfrak{E}, \mathfrak{q}\big\} = \mathrm{Arg}\Big\{\inf_{\mathfrak{E}, \mathfrak{q}} \pi(\mathfrak{E}, \mathfrak{q})\Big\} \tag{20}$$

can be formulated as a pure minimization problem.[1]

Since the external contribution in the potential in (10) is independent of the internal state variables, their incremental update can be performed independently by optimizing the variational sub-problem

$$\mathfrak{q} = \mathrm{Arg}\Big\{\inf_{\mathfrak{q}} \pi^{int}(\mathfrak{E}, \mathfrak{q})\Big\}\,. \tag{21}$$

An optimal state of the internal variables has to fulfill the stationarity condition $\delta_{\mathfrak{q}}\pi^{int} = \boldsymbol{0}$ of the argument in (21). The resulting Euler equations

$$\partial_{\mathfrak{q}}\Psi(\mathfrak{E}, \mathfrak{q}) + \Delta t \partial_{\mathfrak{q}}\Phi\big(\tfrac{1}{\Delta t}(\mathfrak{q} - \mathfrak{q}_n)\big) = 0 \tag{22}$$

are commonly referred to as the *Biot equations* (Biot, 1965) and can be identified with the help of the specific form of the dissipation potential in (17) as the constitutive equations

$$\boldsymbol{f}^A = -\partial_{\boldsymbol{A}}\Psi \qquad \text{and} \qquad \vec{f}^{\rho} = -\partial_{\vec{\rho}}\Psi \tag{23}$$

for the internal driving forces. Their exact expressions are derived from (14) and are given in Sutter (2024).

The remaining part of the optimization problem initially introduced in (20) with respect to the set of independent variables $\mathfrak{E}$ then results in the constitutive variational principle

$$\mathfrak{E} = \mathrm{Arg}\Big\{\inf_{\mathfrak{E}} \big\{W(\mathfrak{E}) - \mathcal{P}^{ext}(\mathfrak{E})\big\}\Big\} \tag{24}$$

by introducing the reduced incremental internal work potential

$$W(\mathfrak{E}) = \inf_{\mathfrak{q}} \big\{\pi^{int}(\mathfrak{E}, \mathfrak{q})\big\} \tag{25}$$

[1] If the electric field is chosen as the independent variable instead of the electric displacement in (5), the resulting variational problem in (20) has a convex-concave saddle-point structure, see e.g. Miehe et al. (2011).

evaluated for a found optimal state of the internal variables. By computing the corresponding stationarity conditions of the variational problem in (24), the general expression

$$\mathfrak{S} = \partial_{\mathfrak{E}} W(\mathfrak{E}) \tag{26}$$

of the constitutive equations for the evaluation of the dependent variables initially introduced in (5) is obtained.

The consistent algorithmic material tangent modulus

$$\mathbb{C}_T := \partial_{\mathfrak{E}} \mathfrak{S} = \partial^2_{\mathfrak{E}\mathfrak{E}} W(\mathfrak{E}) \tag{27}$$

at time t_{n+1} can be calculated analytically by computing the second order derivatives of the reduced incremental internal work potential (25). Due to the introduced incremental variational structure of the local problem at a material point, the material tangent is symmetric for arbitrary processes. The definition of the rate-type potential (10) in terms of the convex Helmholtz free energy Ψ and the assumption of a convex dissipation potential Φ satisfies a non-negative algorithmic representation of the second-order work expression

$$\Delta\mathfrak{S} \cdot \Delta\mathfrak{E} = \Delta\mathfrak{E} \cdot \mathbb{C}_T \cdot \Delta\mathfrak{E} \geq 0\,, \qquad \text{for all} \qquad \Delta\mathfrak{E} \neq \mathbf{0}\,, \tag{28}$$

by a positive definite material tangent modulus and thus ensures a stable electro-mechanical material behavior with unique constitutive relations in (26).

4.5. Numerical treatment of the local problem

Next, we consider a local problem in a non-linear finite element scheme that must be solved at each Gauss point. Such a Gauss point would be representative of a material point in a continuum, which has been the subject of discussion in the previous section. Such a local problem takes as input the current state of the independent variables $\boldsymbol{\varepsilon}$, $\boldsymbol{\eta}$ and $\mathbf{D}$ as well as a converged state of the internal variables $\mathbf{q}_n$ related to the previous global load step t_n.

By including the dissipation potential (17), the optimization problem in (21) becomes

$$\begin{aligned}\mathbf{q} = \operatorname{Arg}\Big\{ \inf_{\mathbf{q}} \Big\{ \Psi(\boldsymbol{\varepsilon},\boldsymbol{\eta},\mathbf{D},\mathbf{q}) - \Psi_n(\boldsymbol{\varepsilon}_n,\boldsymbol{\eta}_n,\mathbf{D}_n,\mathbf{q}_n) \\ + \sup_{\mathbf{f}^q,\gamma}\big\{\mathbf{f}^{q\,T}(\mathbf{q}-\mathbf{q}_n) - \gamma F(\mathbf{f}^q)\big\} \Big\}\Big\}\,,\end{aligned} \tag{29}$$

obtaining an update of the internal state variables at time t_{n+1}. Here, the Lagrange multiplier is considered in its algorithmic form $\gamma = \Delta t\lambda$. In (29), all quantities are represented in vector–matrix notation, which is further indicated by the use of bold letters, regardless of the tensor order. Thus, the internal state variables are written as

$$\begin{aligned} &\mathbf{q} = \left[\mathbf{A}^T,\, \boldsymbol{\rho}^T\right]^T\,, \\ \text{with}\quad &\mathbf{A} = \left[A_{11}, A_{22}, A_{33}, 2A_{12}, 2A_{23}, 2A_{13}\right]^T \\ \text{and}\quad &\boldsymbol{\rho} = \left[\rho_1, \rho_2, \rho_3\right]^T. \end{aligned} \tag{30}$$

The work conjugated dissipative internal driving forces in vector–matrix notation are given by

$$\begin{aligned} &\mathbf{f}^q = \left[\mathbf{f}^{A\,T},\, \mathbf{f}^{\rho\,T}\right]^T\,, \\ \text{with}\quad &\mathbf{f}^A = \left[f^A_{11}, f^A_{22}, f^A_{33}, f^A_{12}, f^A_{23}, f^A_{13}\right]^T \\ \text{and}\quad &\mathbf{f}^\rho = \left[f^\rho_1, f^\rho_2, f^\rho_3\right]^T. \end{aligned} \tag{31}$$

Furthermore, the vector–matrix representations of the stress and strain quantities are given in Appendix B.

In order to realize a numerical solution process for the optimization problem in (29), a well-known return mapping algorithm is used, cf. Wilkins (1964) and Ortiz and Simo (1986). For a given state of the independent variables $\boldsymbol{\varepsilon}$, $\boldsymbol{\eta}$ and $\mathbf{D}$, by considering the relations in (23) the threshold function F is evaluated assuming constant internal variables $\mathbf{q}$ within the time step Δt. If this trial state of the material violates the threshold function, i.e. $F > 0$, an update of the internal state variables is required. By computing the Jacobian of the variation problem in (29), the stationarity conditions

$$\partial_{\mathbf{a}}\,\pi^{int} = \begin{bmatrix} \partial_{\mathbf{A}}\Psi + \mathbf{f}^A \\ \partial_{\rho}\,\Psi + \mathbf{f}^\rho \\ \mathbf{A} - \mathbf{A}_n - \gamma(\partial_{\mathbf{f}^A} F)^T \\ \boldsymbol{\rho} - \boldsymbol{\rho}_n - \gamma(\partial_{\mathbf{f}^\rho} F)^T \\ -F \end{bmatrix}_{19\times 1} =: \mathbf{R} = \mathbf{0} \tag{32}$$

are derived along with the loading and unloading conditions

$$\gamma \geq 0, \quad F \leq 0, \quad \gamma F = 0 \tag{33}$$

that are satisfied for a possible optimal state of the material. In (32), the notation $\mathbf{a} = [\mathbf{q}^T, \mathbf{f}^{q\,T}, \gamma]^T$ is used. An appropriate solution is then found by using Newton's method, where the stationarity conditions in (32) become the residuum $\mathbf{R}$ of the iteration. An incremental update during the solution process is given by

$$\Delta\mathbf{a} = -(\partial_{\mathbf{a}}\mathbf{R})^{-1}\mathbf{R}\,, \tag{34}$$

where the symmetric tangent matrix in (34) represents the Hessian

$$\partial_{\mathbf{a}}\mathbf{R} := \partial^2_{\mathbf{a}\mathbf{a}}\pi^{int} = \begin{bmatrix} \partial^2_{\mathbf{A}\mathbf{A}}\Psi & \partial^2_{\mathbf{A}\rho}\,\Psi & \mathbf{1}_{6\times6} & \mathbf{0}_{6\times3} & \mathbf{0}_{6\times1} \\ \partial^2_{\rho\mathbf{A}}\Psi & \partial^2_{\rho\rho}\,\Psi & \mathbf{0}_{3\times6} & \mathbf{1}_{3\times3} & \mathbf{0}_{3\times1} \\ \mathbf{1}_{6\times6} & \mathbf{0}_{6\times3} & -\gamma\,\partial^2_{\mathbf{f}^A\mathbf{f}^A}F & \mathbf{0}_{6\times3} & -(\partial_{\mathbf{f}^A}F)^T \\ \mathbf{0}_{3\times6} & \mathbf{1}_{3\times3} & \mathbf{0}_{3\times6} & -\gamma\,\partial^2_{\mathbf{f}^\rho\mathbf{f}^\rho}F & -(\partial_{\mathbf{f}^\rho}F)^T \\ \mathbf{0}_{1\times6} & \mathbf{0}_{1\times3} & -\partial_{\mathbf{f}^A}F & -\partial_{\mathbf{f}^\rho}F & 0 \end{bmatrix} \tag{35}$$

of the variational problem in (29), while $\mathbf{1}_{6\times6} = \operatorname{diag}[1\,1\,1\,1\,1\,1]$. The iteration with incremental update (34) can be terminated if the norm of the residual vector in (32) vanishes in the numerical sense, i.e. $\|\boldsymbol{R}\| = \|\partial_{\mathbf{a}}\pi^{int}\| \leq \mathrm{tol}$.

With a found optimal solution state $\mathbf{a} = \mathbf{a}^*$ at hand, the constitutive update of the dependent variables in (26) is performed with

$$\boldsymbol{\sigma} = \partial_{\varepsilon} W = \mathbf{C}^D\left(\boldsymbol{\varepsilon} - \boldsymbol{\varepsilon}^i\right) + \mathbf{b}^T\,\boldsymbol{\eta} - \mathbf{h}^T\left(\mathbf{D} - \mathbf{P}^i\right) \tag{36}$$

$$\boldsymbol{\tau} = \partial_{\eta} W = \mathbf{b}\,\left(\boldsymbol{\varepsilon} - \boldsymbol{\varepsilon}^i\right) + \mathbf{G}^D\boldsymbol{\eta} - \mathbf{f}^T\left(\mathbf{D} - \mathbf{P}^i\right) \tag{37}$$

$$\mathbf{E} = \partial_{\mathbf{D}} W = -\mathbf{h}\,\left(\boldsymbol{\varepsilon} - \boldsymbol{\varepsilon}^i\right) - \mathbf{f}\,\boldsymbol{\eta} + \boldsymbol{\beta}^{\varepsilon}\left(\mathbf{D} - \mathbf{P}^i\right), \tag{38}$$

while $\mathbf{C}^D$, $\mathbf{b}$, $\mathbf{h}$, $\mathbf{G}^D$, $\mathbf{f}$ and $\boldsymbol{\beta}^{\varepsilon}$ are the vector–matrix representations of the material tensors in (15), see Appendix C. Finally, the symmetric material tangent moduli in (27) can be expressed explicitly as

$$\begin{aligned}\mathbf{C}_T = &\begin{bmatrix} \partial^2_{\varepsilon\varepsilon}W & \partial^2_{\varepsilon\eta}W & \partial^2_{\varepsilon\mathbf{D}}W \\ \partial^2_{\eta\varepsilon}W & \partial^2_{\eta\eta}W & \partial^2_{\eta\mathbf{D}}W \\ \partial^2_{\mathbf{D}\varepsilon}W & \partial^2_{\mathbf{D}\eta}W & \partial^2_{\mathbf{D}\mathbf{D}}W \end{bmatrix} = \begin{bmatrix} \partial^2_{\varepsilon\varepsilon}\Psi & \partial^2_{\varepsilon\eta}\Psi & \partial^2_{\varepsilon\mathbf{D}}\Psi \\ \partial^2_{\eta\varepsilon}\Psi & \partial^2_{\eta\eta}\Psi & \partial^2_{\eta\mathbf{D}}\Psi \\ \partial^2_{\mathbf{D}\varepsilon}\Psi & \partial^2_{\mathbf{D}\eta}\Psi & \partial^2_{\mathbf{D}\mathbf{D}}\Psi \end{bmatrix} \\ &- \begin{bmatrix} \partial^2_{\varepsilon\mathbf{q}}\Psi & \mathbf{0}_{6\times10} \\ \partial^2_{\eta\mathbf{q}}\Psi & \mathbf{0}_{18\times10} \\ \partial^2_{\mathbf{D}\mathbf{q}}\Psi & \mathbf{0}_{3\times10} \end{bmatrix}\left(\partial_{\mathbf{a}}\mathbf{R}\right)^{-1}\begin{bmatrix} \partial^2_{\mathbf{q}\varepsilon}\Psi & \partial^2_{\mathbf{q}\eta}\Psi & \partial^2_{\mathbf{q}\mathbf{D}}\Psi \\ \mathbf{0}_{10\times6} & \mathbf{0}_{10\times18} & \mathbf{0}_{10\times3} \end{bmatrix}, \end{aligned} \tag{39}$$

where the second term is active only if the threshold function (19) is violated and an evolution of the internal state variables takes place. For more details on the implementation of the numerical treatment, see Sutter (2024).

5. Mixed flexoelectric finite element formulation

Due to the occurrence of higher-order derivatives of the displacement field, the consideration of flexoelectricity in an electromechanical theory leads to fourth-order partial differential equations with higher-order boundary conditions for the description of the global boundary value problem. For the numerical solution of such a higher-order problem in the context of the finite element method, special

approximation techniques have to be used which satisfy higher continuity requirements, cf. e.g. Argyris et al. (1968), Dasgupta and Sengupta (1990) and Petera and Pittman (1994). In order to avoid the complexities involved by such formulations, mixed finite element formulations are an alternative, see e.g Shu et al. (1999), Amanatidou and Aravas (2002) and Zybell et al. (2012) for applications in strain gradient theory. In the following section, such a mixed formulation for flexoelectric solids based on a scalar-valued global system potential is derived in a variational form and the resulting element matrices and vectors are given.

5.1. Variational formulation

According to Deng et al. (2017), a mixed variational potential for flexoelectric problems in terms of the convex–concave electric Gibbs energy $G_2(\boldsymbol{\varepsilon}, \boldsymbol{\eta}, \vec{E})$ can be written as

$$\begin{aligned} \Pi(\vec{u}, \boldsymbol{H}, \phi, \lambda) = & \int_{\mathcal{B}} \left(G_2(\boldsymbol{\varepsilon}, \boldsymbol{\eta}, \vec{E}) + \lambda : (\boldsymbol{H} - \vec{u} \otimes \vec{\nabla}) \right) dV \\ & + \Pi^{ext}(\vec{u}, \boldsymbol{H}, \phi) \end{aligned} \tag{40}$$

with

$$\begin{aligned} \Pi^{ext}(\vec{u}, \boldsymbol{H}, \phi) = & - \int_{\mathcal{B}} \vec{b}_{ext} \cdot \vec{u} \, dV - \int_{\partial \mathcal{B}_t} \vec{t}_{ext} \cdot \vec{u} \, dA \\ & - \int_{\partial \mathcal{B}_r} \vec{r}_{ext} \cdot (\boldsymbol{H} \cdot \vec{n}) \, dA + \int_{\partial \mathcal{B}_q} q_{ext} \phi \, dA \,, \end{aligned} \tag{41}$$

where $\vec{b}_{ext}$, $\vec{t}_{ext}$, $\vec{r}_{ext}$ and q_{ext} represent the external sources of the body forces per unit volume, the surface tractions, the higher-order surface tractions and the surface charges. In this formulation, the displacement gradient $\boldsymbol{H}$ is introduced as an independent variable and its relation to the displacement field is enforced by a Lagrange multiplier λ. Furthermore, the strain gradient $\boldsymbol{\eta}$ is expressed in terms of the new introduced displacement gradient, cf. $(2)_1$.

In order to introduce a global system potential that is energetically compatible with the variational framework for the local problem introduced in Section 4, it should be formulated in terms of the convex Helmholtz free energy Ψ. More precisely, in case of dissipative material behavior assumed in Section 4, a formulation in terms of the reduced incremental internal work potential $W(\boldsymbol{\varepsilon}, \boldsymbol{\eta}, \vec{D})$ in (25), derived from the special form of the Helmholtz free energy in (14), should be chosen. Therefore, a suitable mixed variational potential can be written as

$$\begin{aligned} \hat{\Pi}(\vec{u}, \boldsymbol{H}, \vec{D}, \phi, \lambda) = & \int_{\mathcal{B}} \Big(W(\boldsymbol{\varepsilon}, \boldsymbol{\eta}, \vec{D}) + \vec{\nabla}\phi \cdot \vec{D} \\ & + \lambda : (\boldsymbol{H} - \vec{u} \otimes \vec{\nabla}) \Big) \, dV + \Pi^{ext}(\vec{u}, \boldsymbol{H}, \phi) \,, \end{aligned} \tag{42}$$

where compared to the potential in (40), the electric Gibbs energy G_2 is expressed in terms of reduced incremental internal work potential W by considering a partial Legendre transformation that performs a variable change in the electric quantities, cf. Sutter and Kamlah (2023), Gil and Ortigosa (2016) and Mao et al. (2016). Such a modification results in the electric displacement $\vec{D}$ as an additional independent variable in the formulation. The corresponding five-field variational principle is then given by the optimization problem

$$\left\{ \vec{u}, \boldsymbol{H}, \vec{D}, \phi, \lambda \right\} = \operatorname{Arg} \left\{ \inf_{\vec{u}, \boldsymbol{H}, \vec{D}} \sup_{\phi, \lambda} \hat{\Pi}(\vec{u}, \boldsymbol{H}, \vec{D}, \phi, \lambda) \right\} \tag{43}$$

with a saddle-point structure for the determination of the unknown field quantities.

The variation of the global system potential in (42) can be calculated as

$$\begin{aligned} \delta \hat{\Pi} = & \int_{\mathcal{B}} \Big(\partial_{\boldsymbol{\varepsilon}} W : \delta\boldsymbol{\varepsilon} - \lambda : \delta\vec{u} \otimes \vec{\nabla} + \partial_{\boldsymbol{\eta}} W \therefore \delta\boldsymbol{\eta} + \lambda : \delta\boldsymbol{H} \\ & + (\partial_{\vec{D}} W + \vec{\nabla}\phi) \cdot \delta\vec{D} + \vec{D} \cdot \vec{\nabla}\delta\phi + (\boldsymbol{H} - \vec{u} \otimes \vec{\nabla}) : \delta\lambda \Big) \, dV \\ & + \delta\Pi^{ext} \overset{!}{=} 0 \end{aligned} \tag{44}$$

with

$$\begin{aligned} \delta\Pi^{ext} = & - \int_{\mathcal{B}} \vec{b}_{ext} \cdot \delta\vec{u} \, dV - \int_{\partial \mathcal{B}_t} \vec{t}_{ext} \cdot \delta\vec{u} \, dA \\ & - \int_{\partial \mathcal{B}_r} \vec{n} \otimes \vec{r}_{ext} : \delta\boldsymbol{H} \, dA + \int_{\partial \mathcal{B}_q} q_{ext} \delta\phi \, dA \,. \end{aligned} \tag{45}$$

By applying partial integration and the divergence theorem, the associated Euler equations

$$\vec{\nabla} \cdot (\partial_{\boldsymbol{\varepsilon}} W - \lambda) + \vec{b}_{ext} = \vec{0} \quad \text{in } \mathcal{B} \tag{46a}$$

$$\partial_{\boldsymbol{\eta}} W \cdot \vec{\nabla} - \lambda = \boldsymbol{0} \quad \text{in } \mathcal{B} \tag{46b}$$

$$\partial_{\vec{D}} W + \vec{\nabla}\phi = \vec{0} \quad \text{in } \mathcal{B} \tag{46c}$$

$$\vec{\nabla} \cdot \vec{D} = 0 \quad \text{in } \mathcal{B} \tag{46d}$$

$$\boldsymbol{H} - \vec{u} \otimes \vec{\nabla} = \boldsymbol{0} \quad \text{in } \mathcal{B} \tag{46e}$$

$$(\partial_{\boldsymbol{\varepsilon}} W - \lambda) \cdot \vec{n} - \vec{t}_{ext} = \vec{0} \quad \text{on } \partial\mathcal{B}_t \tag{46f}$$

$$\partial_{\boldsymbol{\eta}} W \cdot \vec{n} - \vec{n} \otimes \vec{r}_{ext} = \boldsymbol{0} \quad \text{on } \partial\mathcal{B}_r \tag{46g}$$

$$\vec{D} \cdot \vec{n} + q_{ext} = 0 \quad \text{on } \partial\mathcal{B}_q \tag{46h}$$

are derived from the variational formulation in (44) describing the underlying boundary value problem. In this set of equations, the physical meaning of the Lagrange multiplier, which enforces the kinematic relation in (46e), can be recognized in (46b) as the divergence of the non-local stress (37). Together with the local stress (36), it has to satisfy the balance of linear momentum of a non-local continuum in (46a). Furthermore, besides the relation (4) connecting the electric field with the electric potential in (46c) as well as Gauss law in (46d), the Neumann boundary conditions (46f)–(46h) can be identified.

5.2. Linearization

Due to the assumed non-linearity of the optimization problem in (43), an iterative solution must be performed within the framework of the FEM. The necessary linearization of the variational formulation in (44) can be achieved using the Taylor series expansion $\operatorname{Lin}[\delta\hat{\Pi}(x)] = \delta\hat{\Pi}(x) + D_x[\delta\hat{\Pi}(x)] \cdot \Delta x = \delta\hat{\Pi} + \delta\Delta\hat{\Pi} \approx 0$, cf. e.g. Wriggers (2008). Under the assumption of conservative external loads, the tangential part of the linearization

$$\begin{aligned} \delta\Delta\hat{\Pi} = & \int_{\mathcal{B}} \Big(\delta\boldsymbol{\varepsilon} : (\partial^2_{\boldsymbol{\varepsilon}\boldsymbol{\varepsilon}} W : \Delta\boldsymbol{\varepsilon} + \partial^2_{\boldsymbol{\varepsilon}\boldsymbol{\eta}} W \therefore \Delta\boldsymbol{\eta} + \partial^2_{\boldsymbol{\varepsilon}\vec{D}} W \cdot \Delta\vec{D}) \\ & + \delta\boldsymbol{\eta} \therefore (\partial^2_{\boldsymbol{\eta}\boldsymbol{\varepsilon}} W : \Delta\boldsymbol{\varepsilon} + \partial^2_{\boldsymbol{\eta}\boldsymbol{\eta}} W \therefore \Delta\boldsymbol{\eta} + \partial^2_{\boldsymbol{\eta}\vec{D}} W \cdot \Delta\vec{D}) \\ & - \delta\vec{u} \otimes \vec{\nabla} : \Delta\lambda + \delta\boldsymbol{H} : \Delta\lambda \\ & + \delta\vec{D} \cdot (\partial^2_{\vec{D}\boldsymbol{\varepsilon}} W : \Delta\boldsymbol{\varepsilon} + \partial^2_{\vec{D}\boldsymbol{\eta}} W \therefore \Delta\boldsymbol{\eta} + \partial^2_{\vec{D}\vec{D}} W \cdot \Delta\vec{D} + \vec{\nabla}\Delta\phi) \\ & + \vec{\nabla}\delta\phi \cdot \Delta\vec{D} + \delta\lambda : \Delta\boldsymbol{H} - \delta\lambda : \Delta\vec{u} \otimes \vec{\nabla} \Big) \, dV \end{aligned} \tag{47}$$

is derived. The occurring components of the material tangent in (47) are given in (39).

5.3. Discretization

In the following, we assume a discretized problem with a subdivision of the continuous body under consideration into a finite number n_{elem} of elements. In order to define appropriate shape functions for an isoparametric finite element formulation, the admissible functional spaces for the individual field quantities must be identified first.

For the displacement field, a functional space satisfying the corresponding Dirichlet boundary conditions with their predefined values $\square^*$ is given by

$$\vec{u} \in \mathcal{W}_u := \left\{ \vec{u} \in H^1(\mathcal{B}) \mid \vec{u} = \vec{u}^* \text{ auf } \partial\mathcal{B}_u \right\}, \tag{48}$$

which corresponds to the Sobolev space H^1 containing square-integrable functions with existing square-integrable derivatives. Considering the requirements in (48), in this work the approximation of

the displacement field is realized by C^0-continuous quadratic Lagrange polynomials of the serendipity type, cf. e.g. Zienkiewicz et al. (2005). In a compact way, the element-wise interpolation of the displacement field and its gradient can be written as the sums

$$\mathbf{u}^h = \sum_{I=1}^{n_{el}^u} \mathbf{N}_I^u \mathbf{u}_I = \mathbf{N}_e^u \mathbf{u}_e \quad \text{and} \quad \nabla \mathbf{u}^h = \sum_{I=1}^{n_{el}^u} \mathbf{M}_I^u \mathbf{u}_I = \mathbf{M}_e^u \mathbf{u}_e \tag{49}$$

over the corresponding element nodes $n_{el}^{\square}$ in terms of the nodal values $\mathbf{u}_I$, while the approximation of the strain field reads

$$\boldsymbol{\varepsilon}^h = \sum_{I=1}^{n_{el}^u} \mathbf{B}_I^u \mathbf{u}_I = \mathbf{B}_e^u \mathbf{u}_e \,. \tag{50}$$

The nodal matrices of the shape functions $\mathbf{N}_I^u$ and their derivatives $\mathbf{B}_I^u$ and $\mathbf{M}_I^u$, as well as those introduced in the same fashion subsequently, are given in detail in Sutter (2024). For the discretized fields $\square^h$ again a vector–matrix notation is used in this section, indicated by bold symbols.

Similar to the displacement field, the requirements

$$\phi \in \mathcal{W}_\phi := \left\{ \phi \in H^1(\mathcal{B}) \mid \phi = \phi^* \text{ auf } \partial\mathcal{B}_\phi \right\} \tag{51}$$

for the functional space of the electric potential are also satisfied by using C^0-continuous quadratic serendipity Lagrange polynomials for the construction

$$\phi^h = \sum_{I=1}^{n_{el}^\phi} N_I^\phi \phi_I = \mathbf{N}_e^\phi \boldsymbol{\phi}_e \quad \text{and} \quad \nabla \phi^h = \sum_{I=1}^{n_{el}^\phi} \mathbf{B}_I^\phi \phi_I = \mathbf{B}_e^\phi \boldsymbol{\phi}_e \tag{52}$$

of its discretized version and that of its gradient.

For the independent displacement gradient, the admissible functional space

$$\boldsymbol{H} \in \mathcal{W}_H := \left\{ \boldsymbol{H} \in H^1(\mathcal{B}) \mid \boldsymbol{H} \cdot \vec{n} = (\boldsymbol{H} \cdot \vec{n})^* \text{ auf } \partial\mathcal{B}_H \right\} \tag{53}$$

must be taken into account. In accordance with the polynomial degree of the displacement field, its approximation and that of the strain gradient

$$\mathbf{H}^h = \sum_{I=1}^{n_{el}^H} \mathbf{N}_I^H \mathbf{H}_I = \mathbf{N}_e^H \mathbf{H}_e \quad \text{and} \quad \boldsymbol{\eta}^h = \sum_{I=1}^{n_{el}^H} \mathbf{B}_I^H \mathbf{H}_I = \mathbf{B}_e^H \mathbf{H}_e \tag{54}$$

is implemented by a C^0-continuous interpolation with linear Lagrange polynomials, cf. e.g. Wriggers (2008) and Zienkiewicz et al. (2005).

The approximation of the remaining two field quantities, namely the electric displacement and the Lagrange multiplier, must fit into the spaces

$$\begin{aligned} &\vec{D} \in \mathcal{W}_D := \left\{ \vec{D} \in L^2(\mathcal{B}) \right\} \\ \text{and} \quad &\lambda \in \mathcal{W}_\lambda := \left\{ \lambda \in L^2(\mathcal{B}) \right\}, \end{aligned} \tag{55}$$

where L^2 denotes the Lebesgue space of square-integrable functions. This is met by using linear Lagrange polynomials for the interpolation of both fields. In contrast to the Lagrange multiplier, where C^0-continuity is chosen, we use a C^{-1}-continuous (discontinuous) ansatz for the electric displacement. The discretized fields are then given by

$$\mathbf{D}^h = \sum_{I=1}^{n_{el}^D} \mathbf{N}_I^D \mathbf{D}_I = \mathbf{N}_e^D \mathbf{D}_e \quad \text{and} \quad \boldsymbol{\Lambda}^h = \sum_{I=1}^{n_{el}^\lambda} \mathbf{N}_I^\lambda \boldsymbol{\Lambda}_I = \mathbf{N}_e^\lambda \boldsymbol{\Lambda}_e \,. \tag{56}$$

According to the chosen polynomial degrees, the corresponding number of nodes per element involved in the approximation of the degrees of freedom is given, e.g. for a 2D quadrilateral element as $n_{el}^u = n_{el}^\phi = 8$, $n_{el}^H = n_{el}^D = n_{el}^\lambda = 4$ and for a 3D hexahedral element with $n_{el}^u = n_{el}^\phi = 20$, $n_{el}^H = n_{el}^D = n_{el}^\lambda = 8$. Following a classical Bubnov–Galerkin approach, the same shape functions are used for the virtual $\delta\square$ and the incremental $\Delta\square$ representations of all quantities. The vector–matrix representations of the nodal degrees of freedom of the finite element formulation under discussion are given in Appendix D.

By inserting the discretized and approximated quantities introduced in (49), (50), (52), (54) and (56) into the linearized variational formulation by an element-wise consideration of (44) and (47), we end up with the equations

$$\text{Lin}[\delta\hat{\Pi}]_e^h = \delta\hat{\Pi}_e^h + \delta\Delta\hat{\Pi}_e^h = \delta\mathbf{v}_e^T \left(\mathbf{F}_e - \mathbf{P}_e + \mathbf{K}_{Te} \Delta\mathbf{v}_e \right), \tag{57}$$

with the incremental update of the unknown element degrees of freedom

$$\Delta\mathbf{v}_e = \left[\Delta\mathbf{u}_e \quad \Delta\mathbf{H}_e \quad \Delta\mathbf{D}_e \quad \Delta\boldsymbol{\phi}_e \quad \Delta\boldsymbol{\Lambda}_e \right]^T, \tag{58}$$

the components of the element tangential stiffness matrix

$$\mathbf{K}_{Te} = \begin{bmatrix} \mathbf{K}_e^{uu} & \mathbf{K}_e^{uH} & \mathbf{K}_e^{uD} & \mathbf{0} & -\mathbf{K}_e^{u\lambda} \\ \mathbf{K}_e^{Hu} & \mathbf{K}_e^{HH} & \mathbf{K}_e^{HD} & \mathbf{0} & \mathbf{K}_e^{H\lambda} \\ \mathbf{K}_e^{Du} & \mathbf{K}_e^{DH} & \mathbf{K}_e^{DD} & \mathbf{K}_e^{D\phi} & \mathbf{0} \\ \mathbf{0} & \mathbf{0} & (\mathbf{K}_e^{D\phi})^T & \mathbf{0} & \mathbf{0} \\ -(\mathbf{K}_e^{u\lambda})^T & (\mathbf{K}_e^{H\lambda})^T & \mathbf{0} & \mathbf{0} & \mathbf{0} \end{bmatrix}, \tag{59}$$

the element vector of the internal forces

$$\mathbf{F}_e = \begin{bmatrix} \mathbf{F}_e^u & \mathbf{F}_e^H & \mathbf{F}_e^D & \mathbf{F}_e^\phi & \mathbf{F}_e^\lambda \end{bmatrix}^T \tag{60}$$

and the element vector of the external forces

$$\mathbf{P}_e = \begin{bmatrix} \mathbf{P}_e^u & \mathbf{P}_e^H & \mathbf{0} & -\mathbf{P}_e^\phi & \mathbf{0} \end{bmatrix}^T. \tag{61}$$

The different components in (59), (60) and (61) are given in detail in Appendix E. The numerical evaluation of the integrals is performed by standard Gaussian quadrature integration.

Due to the discontinuous approximation of the electric displacement field, a static condensation of the components of this nodal degree of freedom on element level is possible. By considering the third equation in (57) and solving $\text{Lin}[\delta\hat{\Pi}_e]_D = 0$ for arbitrary $\delta\mathbf{D}_e$, the expression

$$\Delta\mathbf{D}_e = -(\mathbf{K}_e^{DD})^{-1} (\mathbf{K}_e^{Du} \Delta\mathbf{u}_e + \mathbf{K}_e^{DH} \Delta\mathbf{H}_e + \mathbf{K}_e^{D\phi} \Delta\boldsymbol{\phi}_e + \mathbf{F}_e^D) \tag{62}$$

is found for its incremental update in terms of the other degrees of freedom. Insertion of (62) into the first, second and fourth equation in (57) leads to the reduced expression

$$\text{Lin}[\delta\hat{\Pi}]_e^h = \delta\tilde{\mathbf{v}}_e^T \left(\tilde{\mathbf{F}}_e - \tilde{\mathbf{P}}_e + \tilde{\mathbf{K}}_{Te} \Delta\tilde{\mathbf{v}}_e \right) \tag{63}$$

of the element-wise linearization, where the incremental changes of the remaining degrees of freedom are given by

$$\Delta\tilde{\mathbf{v}}_e = \left[\Delta\mathbf{u}_e \quad \Delta\mathbf{H}_e \quad \Delta\boldsymbol{\phi}_e \quad \Delta\boldsymbol{\Lambda}_e \right]^T. \tag{64}$$

The components of the reduced element tangential stiffness matrix

$$\tilde{\mathbf{K}}_{Te} = \begin{bmatrix} \tilde{\mathbf{K}}_e^{uu} & \tilde{\mathbf{K}}_e^{uH} & \tilde{\mathbf{K}}_e^{u\phi} & -\mathbf{K}_e^{u\lambda} \\ \tilde{\mathbf{K}}_e^{Hu} & \tilde{\mathbf{K}}_e^{HH} & \tilde{\mathbf{K}}_e^{H\phi} & \mathbf{K}_e^{H\lambda} \\ \tilde{\mathbf{K}}_e^{\phi u} & \tilde{\mathbf{K}}_e^{\phi H} & \tilde{\mathbf{K}}_e^{\phi\phi} & \mathbf{0} \\ -(\mathbf{K}_e^{u\lambda})^T & (\mathbf{K}_e^{H\lambda})^T & \mathbf{0} & \mathbf{0} \end{bmatrix}, \tag{65}$$

the reduced element vector of the internal forces

$$\tilde{\mathbf{F}}_e = \begin{bmatrix} \tilde{\mathbf{F}}_e^u & \tilde{\mathbf{F}}_e^H & \tilde{\mathbf{F}}_e^\phi & \mathbf{F}_e^\lambda \end{bmatrix}^T \tag{66}$$

and the reduced element vector of the external forces

$$\tilde{\mathbf{P}}_e = \begin{bmatrix} \mathbf{P}_e^u & \mathbf{P}_e^H & -\mathbf{P}_e^\phi & \mathbf{0} \end{bmatrix}^T \tag{67}$$

are given in Appendix F. Assembling the incremental equation in (63) over all the elements and assuming arbitrary and non-vanishing variations $\delta\square$, one obtains the linear system of equations

$$\bigcup_{e=1}^{n_{elem}} \delta\tilde{\mathbf{v}}_e^T \left(\tilde{\mathbf{K}}_{Te} \Delta\tilde{\mathbf{v}}_e + (\tilde{\mathbf{F}}_e - \tilde{\mathbf{P}}_e) \right) = 0 \quad \Longrightarrow \quad \tilde{\mathbf{K}}_T \Delta\tilde{\mathbf{v}} = -\tilde{\mathbf{G}} \tag{68}$$

for the nodal degrees of freedom on the global system level. The recalculation (62) of the condensed nodal electric displacements is performed in each iteration step on the element level with the stored element matrices and vectors from the previous iteration step. Further details on the implementation of the proposed mixed finite element formulation can be found in Sutter (2024).

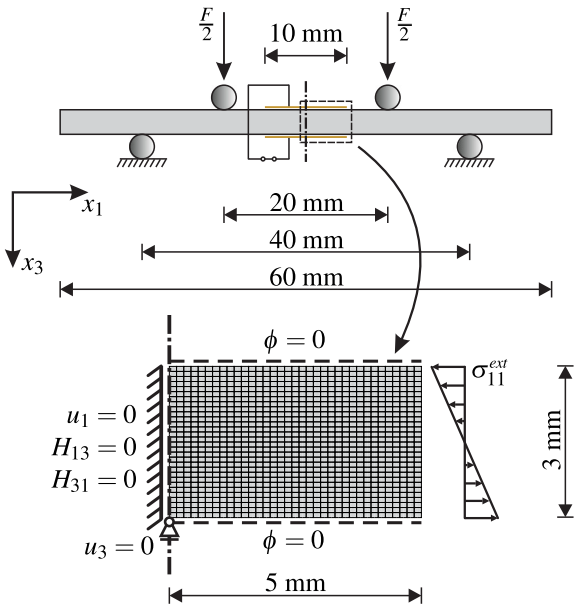

Fig. 2. Top: Sketch of the experimental setup of the four point bending test performed by Ma and Cross (2003). Bottom: 2D plane strain FE model with the specified boundary conditions of the beam section under consideration.

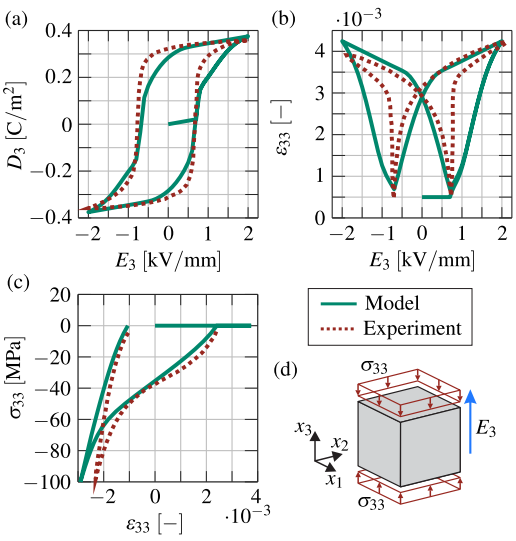

Fig. 3. The adapted dielectric (a) and butterfly hysteresis (b), as well as the ferroelastic behavior (c) calculated using the macroscopic model at a material point representative for a unit volume (d), compared with the experimental results obtained by Chaplya and Carman (2001) for the piezoceramic PZT-5H.

6. Numerical investigations

With the introduced macroscopic model combining ferroelectricity and flexoelectricity, numerical investigations are carried out in the following. In a first step, the model is adapted to the real material behavior by comparison with experimental results of the macroscopic flexoelectric response of ferroelectric ceramics. Furthermore, the adapted model is used to investigate the formation of flexoelectricity-driven remanent polarization in the presence of pronounced strain gradients. The simulations are performed with an in-house FE code in MATLAB (2022).

6.1. Four point bending test

To apply the modeling framework that was previously introduced in the Sections 3 to 5, we will consider an experiment that was carried out by Ma and Cross and documented in Ma and Cross (2003). They performed four point bending tests on samples with the dimensions of 60 mm × 7 mm × 3 mm to investigate the macroscopic occurrence of the direct flexoelectric effect in ferroelectrics. The material under consideration is the commercial piezoceramic PZT-5H manufactured by TRS Ceramics Company, State College, Pennsylvania (USA), in a unpoled state that usually occurs after sintering during the manufacturing process. The corresponding experimental setup is sketched in Fig. 2. The choice of a four point bending test to investigate the flexoelectric effect is reasonable because of the homogeneous bending state without the influence of shear forces in the specimen in the area between the load application points. This allows the assumption of a constant strain gradient component η_{113} in the specimen for the evaluation of the macroscopic flexoelectric response. The polarization that is caused can be estimated by the measurement of the surface charges on the electrodes. The displacement-controlled loading speed chosen in the experiment is 2 mm/min, so that the restriction made in this paper to consider only quasi-static processes applies.

In order to simulate the bending test realistically and at the same time efficiently, a symmetrized two-dimensional plane strain model of the 10 mm wide section with applied electrodes in between the loading points is chosen. Therefore, the 2D model corresponds to a strip cut from the center of the x_2-direction of the beam. In Fig. 2 the half-model selected for the calculation, discretized with 35 × 30 = 1050 finite elements, is illustrated together with the chosen boundary conditions. The bending moment is applied by the external traction σ_{11}^{ext} corresponding to the local stress tensor (cf. (13)), which varies linearly over the beam height. The boundary loaded by σ_{11}^{ext} is sufficiently far away from the symmetry plane that any inhomogeneities due to higher-order stress effects resulting from local load application can be assumed not to affect the region of interest. Thus, at the symmetry plane, the desired homogeneous bending condition is achieved.

Before the simulation of the four point bending test is performed, the parameters of the ferroelectric material model introduced in Section 4 are first adjusted to the real material behavior of PZT-5H, except for the flexoelectric material constants. For this purpose, the results of the experimental investigations of Chaplya and Carman (2001) on the characteristic hysteretic material behavior of this piezoceramic are considered. The hystereses calculated with the model, adapted to the experimental material behavior, are shown in Fig. 3. The dielectric hysteresis, the butterfly hysteresis and the ferroelastic behavior during a mechanical depolarization process have been taken into account. A simplified model variant neglecting the flexoelectric effect was assumed in the calculations performed on an isolated material point in the course of the adaptation process. The parameters for which the calculated response of the material model could be adequately matched to the real large-signal behavior of the piezoceramic are listed in Table 1.

The next step is the repeated simulation of the four point bending test with varying the flexoelectric constants m_{12} and m_{44} to match as closely as possible the macroscopic flexoelectric response observed by Ma and Cross (2003). In order to minimize the impact of the strain gradient elasticity on the model response, we set the internal length parameter l_e (see (A.3)) to a relatively low value,[2] cf. Table 1. In the non-linear finite element calculations, the external bending stress is applied in ten equidistant loading and five unloading steps with a maximum magnitude of $\sigma_{11}^{ext,max} = 60$ MPa. At the beginning of each simulation, the material of the sample is assumed to be in a thermally depolarized state, cf. Section 3.2. The comparison of the fitted simulation results with the experimental data is presented in

[2] Choosing $l_e = 0$ would lead to a non-positive definite material matrix in (39) and therefore to an unstable material behavior.

Table 1
Parameters of the material model introduced in Section 4 for the four point bending test adapted to the large signal behavior of the commercial piezoceramic PZT-5H (cf. also Appendix A).

Parameter	Value	Calc. value
Y	70000 MPa	70 kN/mm^2
ν	0.31	0.31
l_e	$1 \cdot 10^{-9}$ m	$1 \cdot 10^{-6}$ mm
d_{33}	$0.59 \cdot 10^{-9}$ m/V	0.59 mm/MV
d_{31}	$-0.27 \cdot 10^{-9}$ m/V	−0.27 mm/MV
d_{15}	$0.74 \cdot 10^{-9}$ m/V	0.74 mm/MV
ϵ_0[a]	$8.854 \cdot 10^{-12}$ C/(V m)	$8.854 \cdot 10^{-3}$ kN/MV^2
κ^σ	$30 \cdot 10^{-9}$ C/(V m)	30 kN/MV^2
m_{12}	$5 \cdot 10^{-8}$ C/m	$5 \cdot 10^{-5}$ kN/MV
m_{44}	$-1.1 \cdot 10^{-6}$ C/m	$-1.1 \cdot 10^{-3}$ kN/MV
E^c	$0.7 \cdot 10^{6}$ V/m	$0.7 \cdot 10^{-3}$ MV/mm
σ^c	25 MPa	$25 \cdot 10^{-3}$ kN/mm^2
P^{sat}	0.37 C/m^2	0.37 kN/(MV mm)
ϵ^{sat}	0.0035	0.0035
c_A	0.25 MPa	$2.5 \cdot 10^{-4}$ kN/mm^2
c_ρ	$1 \cdot 10^{-3}$ MPa	$1 \cdot 10^{-6}$ kN/mm^2
a_A	$1 \cdot 10^{-3}$ MPa	$1 \cdot 10^{-6}$ kN/mm^2
m_A	0.8	0.8
a_ρ	$5 \cdot 10^{-3}$ MPa	$5 \cdot 10^{-6}$ kN/mm^2
m_ρ	0.6	0.6
ξ	0.2	0.2

[a] Natural constant.

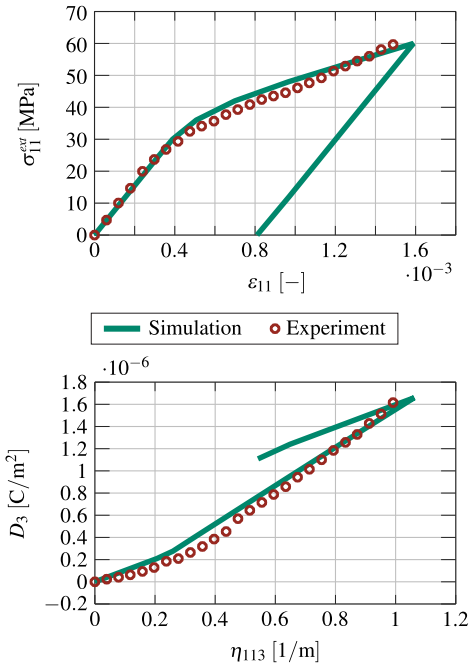

Fig. 4. Comparison of the results of the FE calculation with the experimentally determined quasi-static system behavior of the 4-point bending test at a displacement controlled loading rate of 2 mm/min. Top: Applied external bending stress σ_{11}^{ext} over axial strain of the bottom edge fibers of the beam ε_{11}. Bottom: Vertical component of the electric displacement D_3 over the gradient in vertical x_3-direction η_{113} of the axial strain.

Fig. 4. The upper diagram shows the evolution of the axial strain component of the bottom edge fibers of the beam in response to the external bending stress during the loading and unloading process. The pronounced deviation from initial linearity can be attributed to the occurrence of ferroelastic domain switching. This process begins at a bending stress level of around 30 MPa and results in a significant reduction in beam stiffness, which is well replicated by the model. At the end of the linear-elastic unloading path of the model response, a remanent strain of approximately 0.08% is observed. This is consistent with the experimental observation of a residual curvature in the sample after unloading, cf. Cross (2006).

For the quantification of the direct flexoelectric effect, the focus in the lower diagram in Fig. 4 is on the vertical component of the electric displacement caused by the acting strain gradient component η_{113}. The predicted model response is also compared to the experimental results. From Gauss's law together with the 'closed circuit' boundary condition it follows that the dielectric displacement is constant over the beam height. Likewise, η_{113} is constant in this direction since the axial strain is linear caused by the pure bending state. With the adjusted flexoelectric constants given in Table 1, the model can represent the change in slope that correlates with the onset of the ferroelastic domain switching processes. According to Zubko et al. (2007), the effective transverse flexoelectric coefficient

$$m_{12}^{eff} = m_{12} - \frac{\nu}{1-\nu}(m_{12} + 2m_{44}) = 1.02\ \mu\text{C/m} \tag{69}$$

can be calculated based on the adapted flexoelectric tensor components, which can be directly compared with the experimental results. This value lies between the coefficients of 0.5 and 2 μC/m determined piecewise by Ma and Cross (2003) and can therefore be classified as quite realistic. After full load recovery, a strain gradient remains in the sample due to the remanent strains caused by the ferroelastic domain switching. Therefore, a remanent polarization also remains due to the direct flexoelectric coupling. Unfortunately, a comparison of this observation is not possible due to the lack of experimental results of the unloading path.

After successfully adapting the model to the real flexoelectric system behavior, the distribution of the individual field variables along the symmetry axis of the model is now considered. For this purpose, Fig. 5 (top) shows the relevant mechanical and electrical quantities over the x_3-coordinate in the height direction of the beam at the time of the maximum external load $\sigma_{11}^{ext,max} = 60$ MPa. The linearly distributed external bending stress σ_{11}^{ext} results in a linear distribution of the axial strain ε_{11}. This result confirms that the simulations have reproduced the desired pure bending state in the symmetry plane of the model. At this loading state, ferroelastic domain switching processes have already occurred over more than two-thirds of the entire cross section. This can be seen from the appearance of the irreversible strain components ε_{11}^i and ε_{33}^i on the one hand, and the flattening slope of the axial stress σ_{11} on the other. The difference between the maximum axial stress component σ_{11} at the outer edge fibers with the external bending stress σ_{11}^{ext} is caused by the constraint to satisfy the switching criterion (19). Corresponding to the linear axial strain distribution, the strain gradient component η_{113} becomes constant over the cross section. The section-wise linear strain ε_{33} in height direction exhibits kinks due to the dominance of its irreversible components ε_{33}^i. This results in a section-wise constant distribution for the associated strain gradient component η_{333} with local non-linearities located in the regions where the transition from reversible to irreversible material behavior takes place.

According to the flexoelectric transverse effect, a constant downward electric displacement D_3 occurs in the height direction of the beam. It is a result of the constant strain gradient component η_{113} and also follows the Gaussian law. An axial component of the electric displacement D_1 in the beam can be excluded by assuming charge-free model boundaries on the left and right sides. The distribution of the electric field, and correspondingly of the electric potential, results from the conditions of satisfying the constitutive equation (38) and, at the same time, resulting in a constant dielectric displacement according to Gauss's law. The maximum electric field strength reached in the cross section is only a few parts per thousand of the coercive field strength. It appears that the irreversible polarization in the outer regions is caused by the local maximum of the strain gradient component η_{333}, which moves during the loading process from the outside to the inside from both, the top and bottom surfaces, and seems to act as an electrical driving force due to the flexoelectric effect.

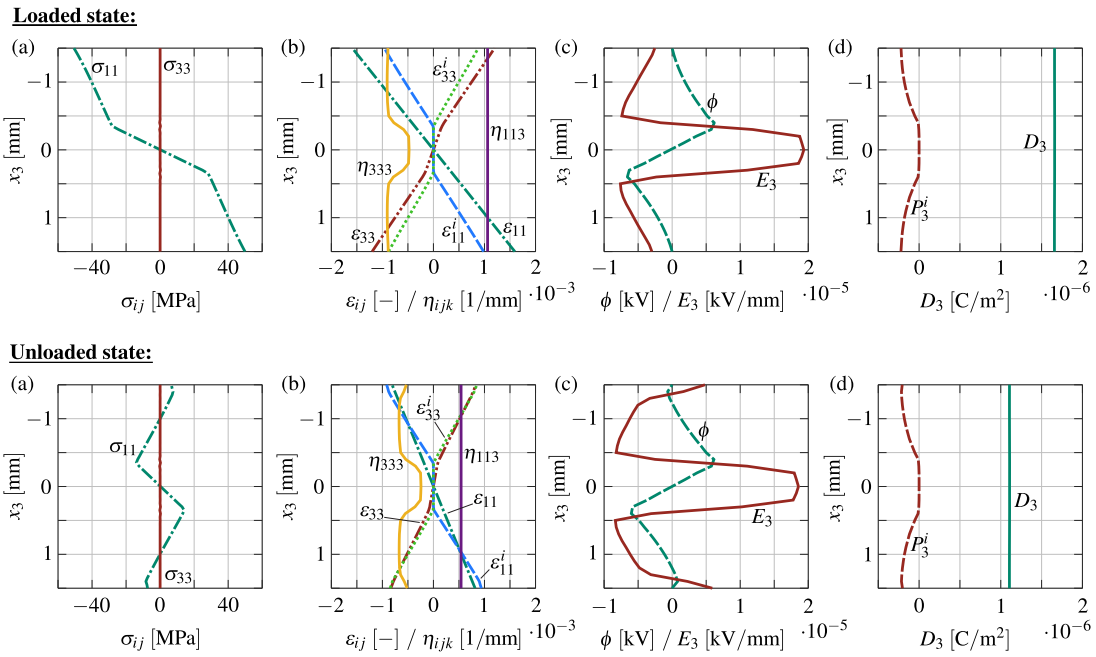

Fig. 5. Results of the individual field quantities along the symmetry axis of the model at the time of the maximum bending stress $\sigma_{11}^{ext,max} = 60$ MPa (top) and after complete unloading (bottom). (a) Stress components (b) Strain and strain gradient components (c) Vertical electric field and potential (d) Vertical components of electric displacement and irreversible polarization.

The results of the considered field quantities after complete unloading of the sample are shown at the bottom of Fig. 5. Due to the ferroelastic switching processes occurring in the specimen, the axial stress σ_{11} cannot be completely relieved and a residual stress state remains in the cross section. The strain components ε_{11} and ε_{33} decrease in amplitude and correspond approximately to their irreversible counterparts after unloading. The strain gradients also decrease in the same way, with an additional decrease at the outer edges of the cross section for the η_{333} component. This effect also has a direct influence on the electric field distribution and the irreversible polarization, where amplitude reductions are also observed in these regions. As can also be seen from the results in Fig. 4, the unloading results in only a slight reduction in the electric displacement in the beam. In the future, the physical plausibility of this observation should be verified as far as possible by further experimental investigations.

6.2. Plate with elliptical notch

In contrast to the previous example, which considered a real experiment, this example is more of an academic problem. The motivation is to select the geometry of a fictitious component in such a way that the direct flexoelectric effect is specifically addressed by strongly pronounced strain gradients. The subject of this investigation is the plate with an elliptical notch in Fig. 6. The geometry of this model problem is taken from Witt et al. (2023), where all dimensions are modified by a factor of 10^{-1}. In this example, plane strain conditions are assumed.

The plate consists of the piezoceramic PZT-5H in the thermally depolarized state, which was already examined in Section 6.1. The flexoelectric, as well as the piezoelectric and ferroelectric properties of this material are accounted for in this example. Therefore, the material parameters from Table 1 are also assumed for this simulation, with the exception of the internal length parameter. The investigations for this example showed a pronounced sensitivity of the numerical calculation stability to this parameter, so that it had to be increased to $l_e = 2 \cdot 10^{-4}$ mm.

The bottom edge of the model is assumed to be mechanically fixed in the x_2-direction and electrically grounded, corresponding to a zero potential. In addition, the center node at the bottom is fixed in the x_1-direction. The purely mechanical load in this example is applied stepwise via a compressive local stress boundary condition[3] at both side faces up to a maximum value of $\sigma_{11}^{max} = 60$ MPa.

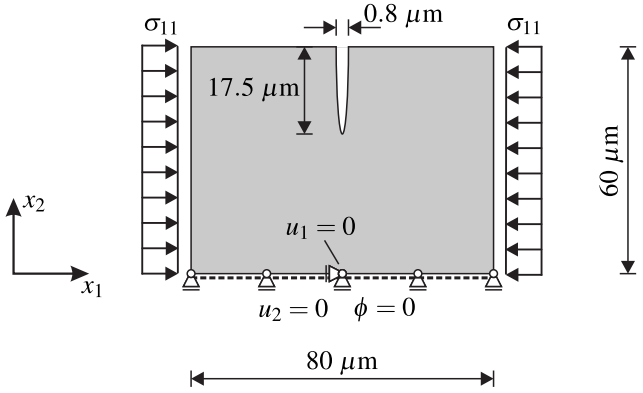

Fig. 6. Model problem of a plate with an elliptical notch and the associated boundary conditions. The notch is not shown to scale.

In this example, high intensity strain gradients are expected in the immediate vicinity of the notch tip. This means that the direct flexoelectric effect can also be expected there. Depending on the intensity of the induced flexoelectric stimulus, electrically driven alignment of the domains in this region can also occur in addition to mechanically driven switching processes. The aim is to investigate the occurrence of the flexoelectric effect and the mechanisms of induced ferroelectricity. For this purpose, the set of material parameters will be used, which are adapted to experiments, see Section 6.1, and therefore are realistic to the best of our knowledge. In particular, we focus on the possibility of

[3] Since it is closer to reality, a compressive instead of a tensile load is considered in this example. Real piezoceramics would be damaged even at very low tensile stresses.

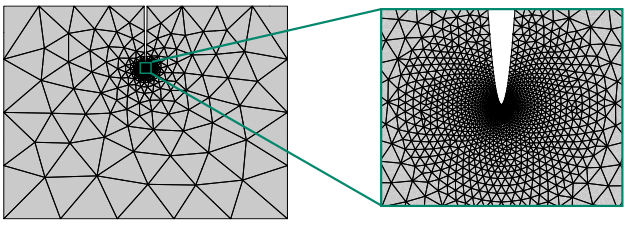

Fig. 7. Selected FE mesh with quadratic triangular elements with a very strong mesh refinement in the area of the notch tip.

gaining a remanent polarization in the material by deliberately creating a strain gradient in the absence of an external electric source.

The simulation is performed on an FE model discretized with 3613 triangular elements[4] with strong mesh refinement in the region of the notch tip, see Fig. 7. The underlying FE formulation corresponds to the one introduced in Section 5. The specified loading of the left and right hand sides is applied in 80 equidistant steps within the FE calculation. The subsequent unloading is also done in 80 steps. These relatively small loading and unloading steps are necessary because of the highly non-linear material behavior that occurs early at the notch tip.

In the following, the results of the simulation at the state of maximum applied compressive stress and after complete unloading are considered. As a result of the applied load, a homogeneous strain state occurs over large areas of the plate. However, strain increases in intensity in the area of the notch. The activation of the flexoelectric effect is caused by the components of the strain gradient tensor. Their distribution at maximum loading in the area of the notch tip is shown in Fig. 8. The selected observation area corresponds to the enlarged area shown in Fig. 7, the dimensions of which are approximately 3×3 μm^2. For better comparability, the same color scale was set for all components shown and limited to reasonable maximum and minimum values. The high intensities of the shear components $2\eta_{121}$ and $2\eta_{122}$ of the strain gradient tensor are striking. Since the adaptation of the flexoelectric constant to the experiment in Section 6.1 resulted in a relatively high value for the shear parameter m_{44}, the field distributions shown in Fig. 8 can be considered as optimal conditions for the activation of the direct flexoelectric effect.

The distribution and strength of the electric field components generated by the direct flexoelectric effect at maximum load are shown in Fig. 9. The maximum values of the selected color scale are limited to the coercive field strength, cf. Table 1. It is clear that this coercivity value is only reached in the immediate vicinity of the notch tip. However, looking at the distribution of the irreversible polarization components in the same figure, it can be seen that domain switching processes and thus poling of the material occurs over a much larger area. The local distribution of the irreversible polarization components can only partially be explained by the shape of the electric field components. Apparently, the strain gradient tensor components play the role of a direct internal driving force in the evolution of the irreversible polarization by the direct flexoelectric effect. This suggests that in the model response discussed here, the electric field is generated more for compatibility reasons to ensure electrostatic equilibrium in the presence of the disturbing flexoelectric effect. The magnitudes of the polarization components are far from reaching the value of the macroscopic saturation polarization resulting from the dielectric hysteresis, cf. Fig. 3. Even at the tip of the notch, the irreversible polarization reaches only about two-thirds of this value, which is not visible in Fig. 9, where the maximum values have also been limited for the sake of clarity.

[4] Triangular elements were chosen because the meshing obtained proved to be much more economical than using quadrilateral elements.

In the following, the focus is on the changes in the field distributions after complete unloading. The components of the strain gradient tensor that remain in the material and are therefore remanent are shown in Fig. 10. Their magnitudes are significantly smaller than at maximum loading, this is why the limits of the color scale have been reduced by a factor of 1/3. The persistence of the strain gradients can be attributed to the inhomogeneous remanent strains caused by ferroelectric and ferroelastic domain switching processes in the region of the notch. Therefore, the flexoelectric effect is expected to persist even after the samples are mechanically unloaded.

The distributions of the irreversible polarization components shown in Fig. 11 are qualitatively similar to those at maximum load. Despite the strong decrease in the strain gradients and thus the magnitude of the flexoelectric effect, the polarization caused in the material does not decrease. The remanent nature of the polarization is therefore evident, as is the poled state of the material at the base of the notch. The electric fields also decrease but do not disappear. They are essentially the depolarization fields that compensate for the polarization remaining in the material.

7. Conclusion

This paper presents a macroscopic continuum model that accounts for the higher-order effect of flexoelectricity in addition to the hysteretic material behavior of piezoceramics. Based on the concept of generalized standard materials, a thermodynamically consistent macroscopic modeling framework for higher-order dissipative electromechanical solids with a minimum-type variational potential structure is established. For the description of the domain switching processes characteristic of ferroelectrics, a microscopically motivated material model is used that is capable of representing the whole relevant range of the quasi-static hysteretic material behavior. To solve the higher-order electro-mechanical boundary value problems arising in flexoelectricity, a mixed finite element formulation based on the Helmholtz free energy is presented. In the numerical examples discussed, the parameters of the non-linear material model are first adapted to the experimentally measured flexoelectric behavior of the piezoceramic PZT-5H in a four point bending test as can be found in literature. This adapted parameter set is then used to calculate a notched plate under compressive loading. Due to the strong strain gradients in the region of the notch tip, domain switching processes and thus polarization of the material can be observed in the model response due to the direct flexoelectric effect. However, this is limited to a small region around the notch tip. Since the calculations were performed with a set of parameters that can be considered quite realistic, this gives at least an indication that such flexoelectricity-driven poling processes can occur in reality. For smaller samples much larger polarized volume fractions in the material can be expected to be affected due to the pronounced size effect of flexoelectricity. The results presented in this work can stimulate further in-depth investigations into the possibility of enhancing the impact of the direct flexoelectric effect and the perspectives of employing it to induce poling processes without an electric source.

CRediT authorship contribution statement

Felix Sutter: Writing – review & editing, Writing – original draft, Visualization, Software, Methodology, Investigation, Formal analysis, Conceptualization. **Marc Kamlah:** Writing – review & editing, Supervision, Project administration, Investigation, Funding acquisition, Conceptualization.

Declaration of competing interest

The authors declare that they have no known competing financial interests or personal relationships that could have appeared to influence the work reported in this paper.

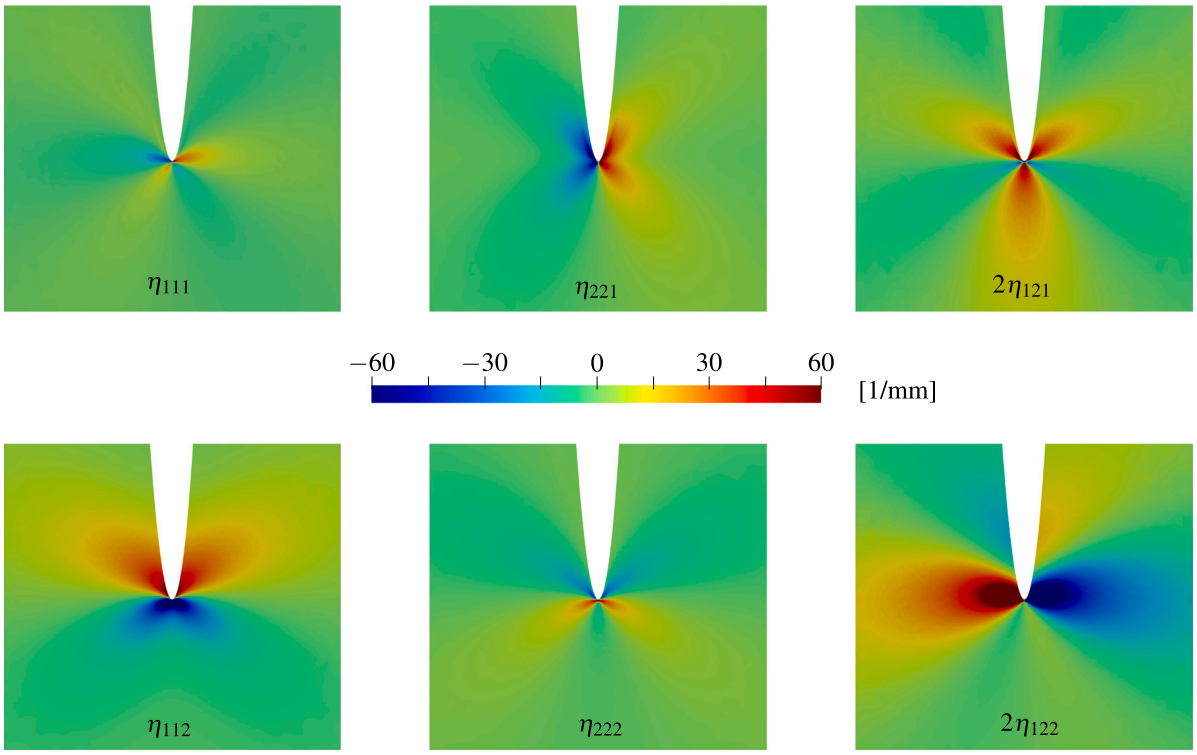

Fig. 8. Distribution of the components of the strain gradient tensor at maximum load in the immediate vicinity of the notch tip. Top: Strain gradients along the horizontal x_1-direction. Bottom: Strain gradients along the vertical x_2-direction. The region of interest corresponds to the detailed view in Fig. 7. (For interpretation of the references to color in this figure legend, the reader is referred to the web version of this article.)

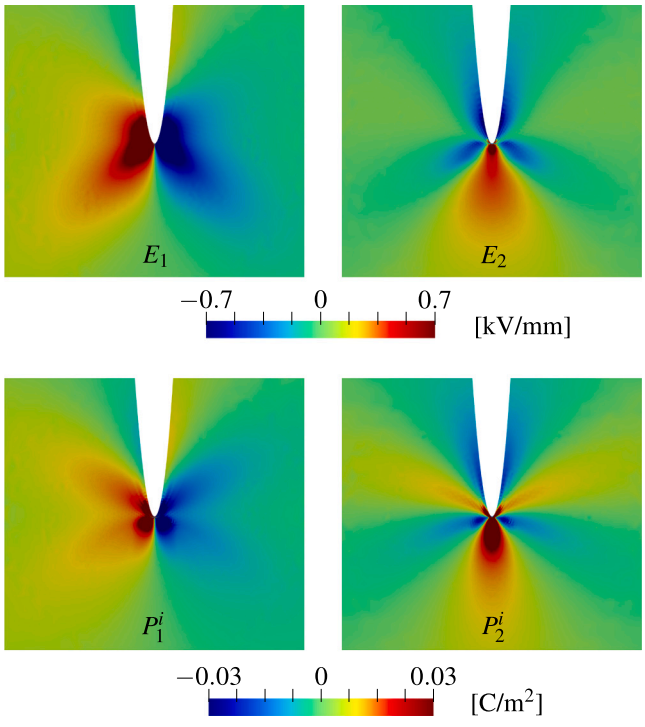

Fig. 9. Distribution of the components of the electric field (top) and the irreversible polarization (bottom) at maximum load in the immediate vicinity of the notch tip. The region of interest corresponds to the detailed view in Fig. 7. (For interpretation of the references to color in this figure legend, the reader is referred to the web version of this article.)

Data availability

Data will be made available on request.

Acknowledgments

The financial support by the Deutsche Forschungsgemeinschaft (DFG) within the project 'Converse Transduction in the Presence of Strong Electrical Field Gradients in Ferroelectrics' (project number: 391065131) is gratefully acknowledged.

Appendix A. Derivation of the Helmholtz free energy

The electric Gibbs energy for a higher-order flexoelectric solid is given by

$$G_2 = \frac{1}{2}\epsilon_{ij}C^E_{ijkl}\epsilon_{kl} + \frac{1}{2}\eta_{ijk}G^E_{ijklmn}\eta_{lmn} - \frac{1}{2}E_i\epsilon^{\varepsilon}_{ij}E_j - E_i e_{ikl}\epsilon_{kl} - E_i m_{ilmn}\eta_{lmn}\,, \tag{A.1}$$

with the isotropic elasticity tensor at constant electric field

$$C^E_{ijkl} = \Lambda\delta_{ij}\delta_{kl} + \mu(\delta_{ik}\delta_{jl} + \delta_{il}\delta_{jk}) \tag{A.2}$$

and the isotropic strain gradient elasticity tensor at constant electric field

$$G^E_{ijklmn} = \Lambda l_e^2\delta_{ij}\delta_{kn}\delta_{lm} + \mu l_e^2(\delta_{il}\delta_{jm}\delta_{kn} + \delta_{im}\delta_{jl}\delta_{kn}) \tag{A.3}$$

expressed in terms of the internal length parameter l_e and the Lamé constants

$$\Lambda = \frac{Y\nu}{(1-2\nu)(1+\nu)} \quad \text{and} \quad \mu = \frac{Y}{2(1+\nu)}\,. \tag{A.4}$$

In (A.4), Y stands for the Young's modulus and ν for the Poisson's ratio. Although piezoceramics exhibit anisotropy, the model was assumed to have isotropic elastic properties for the sake of simplicity.

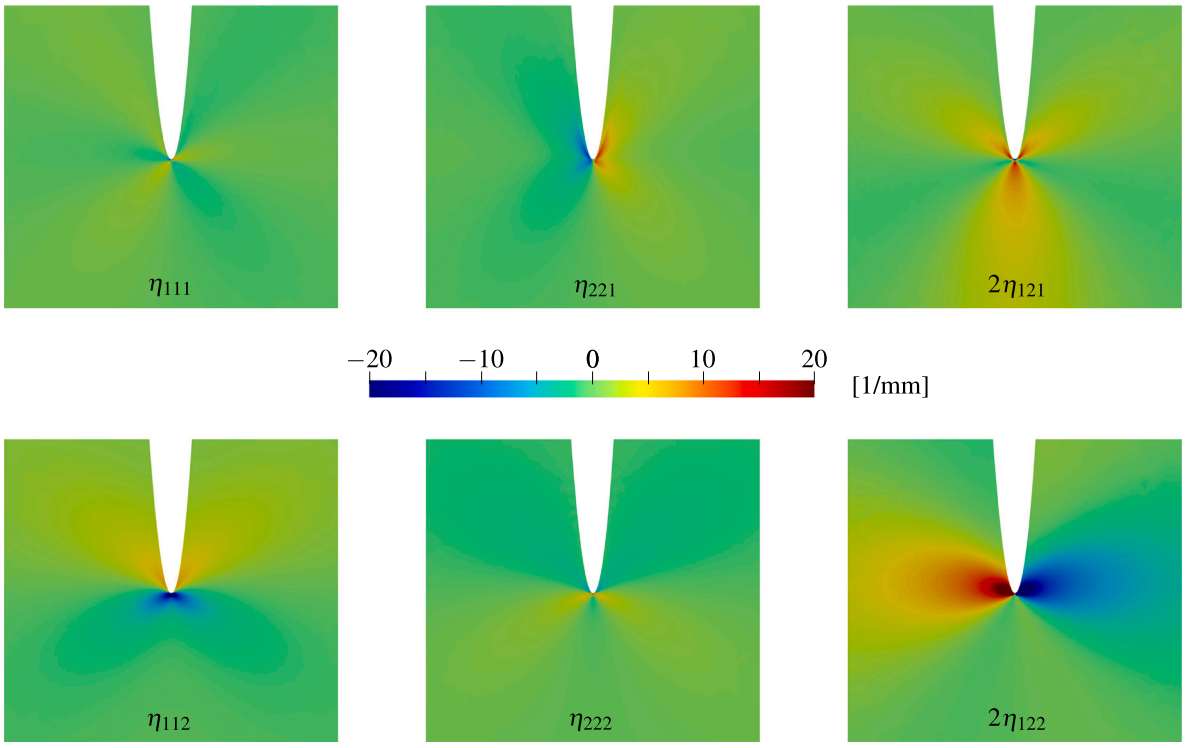

Fig. 10. Distribution of the components of the strain gradient tensor after unloading in the immediate vicinity of the notch tip. Top: Strain gradients along the horizontal x_1-direction. Bottom: Strain gradients along the vertical x_2-direction. The region of interest corresponds to the detailed view in Fig. 7. (For interpretation of the references to color in this figure legend, the reader is referred to the web version of this article.)

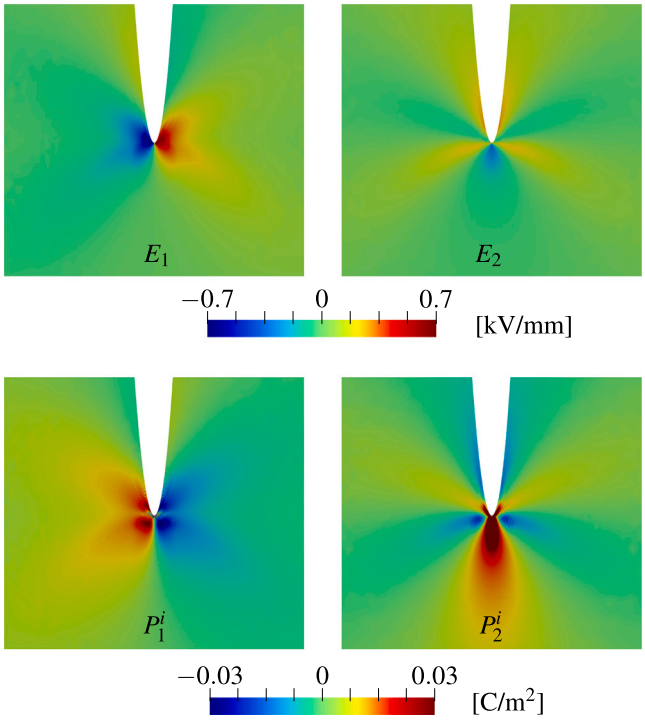

Fig. 11. Distribution of the components of the electric field (top) and the irreversible polarization (bottom) after unloading in the immediate vicinity of the notch tip. The region of interest corresponds to the detailed view in Fig. 7. (For interpretation of the references to color in this figure legend, the reader is referred to the web version of this article.)

The remaining material tensors in (A.1) are the permittivity tensor at constant strain

$$\epsilon_{ij}^{\varepsilon} = \epsilon_{ij}^{\sigma} - d_{ikl} e_{jkl} \,, \tag{A.5}$$

the piezoelectric e-tensor

$$e_{mkl} = d_{mij} C_{ijkl}^{E} \tag{A.6}$$

and the isotropic flexoelectric tensor

$$m_{lijk} = m_{12}\delta_{lk}\delta_{ij} + m_{44}(\delta_{li}\delta_{jk} + \delta_{lj}\delta_{ik}) \,, \tag{A.7}$$

where m_{12} and m_{44} are the transversal and shear flexoelectric coefficients, respectively. Due to the lack of information on the anisotropic properties of the flexoelectric tensor in the literature, an isotropic representation was chosen here for simplicity. In (A.5) and (A.6) one can find the isotropic permittivity tensor at constant stress

$$\epsilon_{ij}^{\sigma} = (\epsilon_0 + \kappa^{\sigma})\delta_{ij} \tag{A.8}$$

and the anisotropic piezoelectric d-tensor

$$\begin{aligned} d_{kij} = {} & \big(d_{33} - d_{31} - d_{15}\big)\rho_k\rho_i\rho_j + d_{31}\rho_k\delta_{ij} \\ & + \frac{1}{2} d_{15}\big(\delta_{ki}\rho_j + \delta_{kj}\rho_i\big) \,, \end{aligned} \tag{A.9}$$

with the additional parameters ϵ_0, κ^{σ} and d_{33}, d_{31}, d_{15} representing the permittivity of the vacuum, the dielectric susceptibility of the material and the longitudinal, transversal and shear piezoelectric constants, respectively.

The constitutive equations in the electric Gibbs energy form can then be derived as

$$\sigma_{ij} = \frac{\partial G_2}{\partial \varepsilon_{ij}} = C_{ijkl}^{E}\varepsilon_{kl} - e_{kij}E_k \,, \tag{A.10}$$

$$\tau_{ijk} = \frac{\partial G_2}{\partial \eta_{ijk}} = G_{ijklmn}^{E}\eta_{lmn} - m_{lijk}E_l \,, \tag{A.11}$$

and

$$D_i = -\frac{\partial G_2}{\partial E_i} = e_{ikl}\varepsilon_{kl} + m_{iklm}\eta_{klm} + \epsilon_{ij}^{\varepsilon}E_j \,. \tag{A.12}$$

By solving (A.12) for the electric field and inserting it into (A.10) and (A.11), the constitutive equations in the Helmholtz free energy scheme become

$$\sigma_{ij} = (C_{ijkl}^{E} + e_{mij}h_{mkl})\varepsilon_{kl} + (f_{klmn}e_{kij})\eta_{lmn} - \big(e_{kij}(\epsilon_{kl}^{\varepsilon})^{-1}\big)D_l$$

$$= C^D_{ijkl}\varepsilon_{kl} + b_{lmnij}\eta_{lmn} - h_{lij}D_l = \frac{\partial \Psi}{\partial \varepsilon_{ij}} \tag{A.13}$$

$$\tau_{ijk} = (m_{lijk}h_{lmn})\varepsilon_{mn} + (G^E_{ijklmn} + m_{oijk}f_{olmn})\eta_{lmn} - \left(m_{lijk}(\epsilon^{\varepsilon}_{lm})^{-1}\right)D_m$$
$$= b_{ijkmn}\varepsilon_{mn} + G^D_{ijklmn}\eta_{lmn} - f_{mijk}D_m = \frac{\partial \Psi}{\partial \eta_{ijk}} \tag{A.14}$$

$$E_i = -\left((\epsilon^{\varepsilon}_{ij})^{-1}e_{jkl}\right)\varepsilon_{kl} - \left((\epsilon^{\varepsilon}_{ij})^{-1}m_{jklm}\right)\eta_{klm} + (\epsilon^{\varepsilon}_{ij})^{-1}D_j$$
$$= -h_{ikl}\varepsilon_{kl} - f_{iklm}\eta_{klm} + \beta^{\varepsilon}_{ij}D_j = \frac{\partial \Psi}{\partial D_i}\,, \tag{A.15}$$

with the impermittivity tensor at constant strain

$$\beta^{\varepsilon}_{ij} = (\epsilon^{\varepsilon}_{ij})^{-1}\,, \tag{A.16}$$

the piezoelectric h-tensor

$$h_{ikl} = \beta^{\varepsilon}_{ij}e_{jkl}\,, \tag{A.17}$$

the elasticity tensor at constant electric displacement

$$C^D_{ijkl} = C^E_{ijkl} + e_{mij}h_{mkl}\,, \tag{A.18}$$

the flexoelectric coupling tensor

$$f_{iklm} = \beta^{\varepsilon}_{ij}m_{jklm}\,, \tag{A.19}$$

the strain gradient elasticity tensor at constant electric displacement

$$G^D_{ijklmn} = G^E_{ijklmn} + m_{oijk}f_{olmn}\,, \tag{A.20}$$

and the strain coupling tensor

$$b_{ijkmn} = m_{lijk}h_{lmn} = m_{lijk}\beta^{\varepsilon}_{lo}e_{omn} = f_{oijk}e_{omn} = b_{ijkmn}\,. \tag{A.21}$$

Finally, the expression for the Helmholtz free energy of a flexoelectric solid of higher-order is found to be

$$\Psi = \frac{1}{2}\varepsilon_{ij}C^D_{ijkl}\varepsilon_{kl} + \frac{1}{2}\eta_{ijk}G^D_{ijklmn}\eta_{klm} + \frac{1}{2}D_i\beta^{\varepsilon}_{ij}D_j$$
$$+ \eta_{ijk}b_{ijklm}\varepsilon_{lm} - D_ih_{ikl}\varepsilon_{kl} - D_if_{iklm}\eta_{klm}\,, \tag{A.22}$$

while its relation to the electric Gibbs energy is given by the partial Legendre transformation

$$G_2(\boldsymbol{\varepsilon}, \boldsymbol{\eta}, \vec{E}) = \inf_{\vec{D}}\left\{\Psi(\boldsymbol{\varepsilon}, \boldsymbol{\eta}, \vec{D}) - \vec{E}\cdot\vec{D}\right\}\,. \tag{A.23}$$

Appendix B. Vector–matrix representations of the mechanical field quantities

The local stress tensor and the strain tensor in a vector–matrix notation are given by

$$\boldsymbol{\sigma} = [\sigma_{11}\ \sigma_{22}\ \sigma_{33}\ \sigma_{12}\ \sigma_{23}\ \sigma_{13}]^T \tag{B.1}$$

$$\boldsymbol{\varepsilon} = [\varepsilon_{11}\ \varepsilon_{22}\ \varepsilon_{33}\ 2\varepsilon_{12}\ 2\varepsilon_{23}\ 2\varepsilon_{13}]^T\,, \tag{B.2}$$

while the notation used in this paper for the non-local stress tensor and the strain gradient tensor is written as

$$\boldsymbol{\tau} = [\tau_{111}\ \tau_{221}\ \tau_{331}\ \tau_{122}\ \tau_{133}\ |\ \tau_{222}\ \tau_{112}\ \tau_{332}\ \tau_{121}\ \tau_{233}\ |$$
$$\tau_{333}\ \tau_{113}\ \tau_{223}\ \tau_{131}\ \tau_{232}\ |\ \tau_{231}\ \tau_{132}\ \tau_{123}]^T \tag{B.3}$$

$$\boldsymbol{\eta} = [\eta_{111}\ \eta_{221}\ \eta_{331}\ 2\eta_{122}\ 2\eta_{133}\ |\ \eta_{222}\ \eta_{112}\ \eta_{332}\ 2\eta_{121}\ 2\eta_{233}\ |$$
$$\eta_{333}\ \eta_{113}\ \eta_{223}\ 2\eta_{131}\ 2\eta_{232}\ |\ 2\eta_{231}\ 2\eta_{132}\ 2\eta_{123}]^T\,. \tag{B.4}$$

Appendix C. Material tensors in vector–matrix notation

The vector–matrix notation of the material tensors is given for the elasticity tensor at constant electric field

$$\mathbf{C}^E = \begin{bmatrix} \Lambda+2\mu & \Lambda & \Lambda & 0 & 0 & 0 \\ \Lambda & \Lambda+2\mu & \Lambda & 0 & 0 & 0 \\ \Lambda & \Lambda & \Lambda+2\mu & 0 & 0 & 0 \\ 0 & 0 & 0 & \mu & 0 & 0 \\ 0 & 0 & 0 & 0 & \mu & 0 \\ 0 & 0 & 0 & 0 & 0 & \mu \end{bmatrix}, \tag{C.1}$$

the strain gradient elasticity tensor at constant electric field

$$\mathbf{G}^E = \begin{bmatrix} \mathbf{G}_1 & \mathbf{0}_{5\times5} & \mathbf{0}_{5\times5} & \mathbf{0}_{5\times3} \\ \mathbf{0}_{5\times5} & \mathbf{G}_1 & \mathbf{0}_{5\times5} & \mathbf{0}_{5\times3} \\ \mathbf{0}_{5\times5} & \mathbf{0}_{5\times5} & \mathbf{G}_1 & \mathbf{0}_{5\times3} \\ \mathbf{0}_{3\times5} & \mathbf{0}_{3\times5} & \mathbf{0}_{3\times5} & \mathbf{G}_2 \end{bmatrix} \tag{C.2}$$

with

$$\mathbf{G}_1 = l_e^2\begin{bmatrix} \Lambda+2\mu & \Lambda & \Lambda & 0 & 0 \\ \Lambda & \Lambda+2\mu & \Lambda & 0 & 0 \\ \Lambda & \Lambda & \Lambda+2\mu & 0 & 0 \\ 0 & 0 & 0 & \mu & 0 \\ 0 & 0 & 0 & 0 & \mu \end{bmatrix} \tag{C.3}$$

and

$$\mathbf{G}_2 = l_e^2\begin{bmatrix} \mu & 0 & 0 \\ 0 & \mu & 0 \\ 0 & 0 & \mu \end{bmatrix}, \tag{C.4}$$

the piezoelectric d-tensor

$$\mathbf{d} = \begin{bmatrix} d_{111} & d_{122} & d_{133} & 2d_{112} & 2d_{123} & 2d_{113} \\ d_{211} & d_{122} & d_{233} & 2d_{212} & 2d_{223} & 2d_{213} \\ d_{311} & d_{322} & d_{333} & 2d_{312} & 2d_{323} & 2d_{313} \end{bmatrix} \tag{C.5}$$

with components d_{kij} of the tensor (A.9), and the flexoelectric tensor

$$\mathbf{m} = \begin{bmatrix} \mathbf{m}_0 & \mathbf{0}_{1\times5} & \mathbf{0}_{1\times5} & \mathbf{0}_{1\times3} \\ \mathbf{0}_{1\times5} & \mathbf{m}_0 & \mathbf{0}_{1\times5} & \mathbf{0}_{1\times3} \\ \mathbf{0}_{1\times5} & \mathbf{0}_{1\times5} & \mathbf{m}_0 & \mathbf{0}_{1\times3} \end{bmatrix} \tag{C.6}$$

with

$$\mathbf{m}_0 = \begin{bmatrix} m_{12}+2m_{44} & m_{12} & m_{12} & m_{44} & m_{44} \end{bmatrix}\,. \tag{C.7}$$

Appendix D. Nodal degrees of freedom of the finite element formulation

The nodal degrees of freedom of the mixed finite element formulation can be summarized as follows:

$$\begin{aligned} \mathbf{u}_I &= [u_1\ u_2\ u_3]^T \\ \mathbf{H}_I &= [H_{11}\ H_{22}\ H_{33}\ H_{12}\ H_{21}\ H_{23}\ H_{32}\ H_{13}\ H_{31}]^T \\ \mathbf{D}_I &= [D_1\ D_2\ D_3]^T \\ \phi_I &= \phi \\ \boldsymbol{\Lambda}_I &= [\lambda_{11}\ \lambda_{22}\ \lambda_{33}\ \lambda_{12}\ \lambda_{21}\ \lambda_{23}\ \lambda_{32}\ \lambda_{13}\ \lambda_{31}]^T \end{aligned} \tag{D.1}$$

Appendix E. Element matrix and vector components of the finite element formulation

The components of the vectors of internal and external forces in (60) and (61) of the proposed finite element formulation are given by

$$\begin{aligned} \mathbf{F}^u_e &= \int_{\Omega_e}\left(\mathbf{B}^{u\,T}_e\partial_{\boldsymbol{\varepsilon}}W - \mathbf{M}^{u\,T}_e\boldsymbol{\Lambda}^h\right)dV\,, \\ \mathbf{P}^u_e &= \int_{\Omega_e}\mathbf{N}^{u\,T}_e\mathbf{b}_{ext}\,dV + \int_{\partial\Omega_e}\mathbf{N}^{u\,T}_e\mathbf{t}_{ext}\,dA\,, \end{aligned} \tag{E.1}$$

$$\begin{aligned} \mathbf{F}^H_e &= \int_{\Omega_e}\left(\mathbf{B}^{H\,T}_e\partial_{\boldsymbol{\eta}}W + \mathbf{N}^{H\,T}_e\boldsymbol{\Lambda}^h\right)dV\,, \\ \mathbf{P}^H_e &= \int_{\partial\Omega_e}\mathbf{N}^{H\,T}_e\mathbf{r}_{ext}\,dA\,, \end{aligned} \tag{E.2}$$

$$\mathbf{F}^D_e = \int_{\Omega_e}\mathbf{N}^{D\,T}_e(\partial_{\mathbf{D}}W + \nabla\phi^h)\,dV\,, \tag{E.3}$$

$$\mathbf{F}^{\phi}_e = \int_{\Omega_e}\mathbf{B}^{\phi\,T}_e\mathbf{D}^h\,dV\,, \qquad \mathbf{P}^{\phi}_e = \int_{\partial\Omega_e}\mathbf{N}^{\phi}_e q_{ext}\,dA\,, \tag{E.4}$$

$$\text{and} \qquad \mathbf{F}^{\lambda}_e = \int_{\Omega_e}\mathbf{N}^{\lambda\,T}_e(\mathbf{H}^h - \nabla\mathbf{u}^h)\,dV\,. \tag{E.5}$$

The components of the tangential stiffness matrix (59) are

$$\begin{aligned} &\mathbf{K}^{uu}_e = \int_{\Omega_e}\mathbf{B}^{u\,T}_e\mathbf{C}^{\varepsilon\varepsilon}_T\mathbf{B}^u_e\,dV\,, \quad \mathbf{K}^{uH}_e = \int_{\Omega_e}\mathbf{B}^{u\,T}_e\mathbf{C}^{\varepsilon\eta}_T\mathbf{B}^H_e\,dV \\ &\mathbf{K}^{uD}_e = \int_{\Omega_e}\mathbf{B}^{u\,T}_e\mathbf{C}^{\varepsilon D}_T\mathbf{N}^D_e\,dV\,, \mathbf{K}^{u\lambda}_e = \int_{\Omega_e}\mathbf{M}^{u\,T}_e\mathbf{N}^{\lambda}_e\,dV \end{aligned} \tag{E.6}$$

$$\mathbf{K}_e^{Hu} = \int_{\Omega_e} \mathbf{B}_e^{H\,T} \mathbf{C}_T^{\eta\varepsilon} \mathbf{B}_e^{u}\, dV\,, \quad \mathbf{K}_e^{HH} = \int_{\Omega_e} \mathbf{B}_e^{H\,T} \mathbf{C}_T^{\eta\eta} \mathbf{B}_e^{H}\, dV$$
$$\mathbf{K}_e^{HD} = \int_{\Omega_e} \mathbf{B}_e^{H\,T} \mathbf{C}_T^{\eta D} \mathbf{N}_e^{D}\, dV\,, \mathbf{K}_e^{H\lambda} = \int_{\Omega_e} \mathbf{N}_e^{H\,T} \mathbf{N}_e^{\lambda}\, dV \tag{E.7}$$

$$\mathbf{K}_e^{Du} = \int_{\Omega_e} \mathbf{N}_e^{D\,T} \mathbf{C}_T^{D\varepsilon} \mathbf{B}_e^{u}\, dV\,, \quad \mathbf{K}_e^{DH} = \int_{\Omega_e} \mathbf{N}_e^{D\,T} \mathbf{C}_T^{D\eta} \mathbf{B}_e^{H}\, dV$$
$$\mathbf{K}_e^{DD} = \int_{\Omega_e} \mathbf{N}_e^{D\,T} \mathbf{C}_T^{DD} \mathbf{N}_e^{D}\, dV\,, \mathbf{K}_e^{D\phi} = \int_{\Omega_e} \mathbf{N}_e^{D\,T} \mathbf{B}_e^{\phi}\, dV\,. \tag{E.8}$$

Appendix F. Components of the reduced tangential stiffness matrix and reduced vector of internal forces

The components of the reduced tangential stiffness matrix are given by

$$\tilde{\mathbf{K}}_e^{uu} = \mathbf{K}_e^{uu} - \mathbf{K}_e^{uD}(\mathbf{K}_e^{DD})^{-1}\mathbf{K}_e^{Du}\,, \tag{F.1}$$

$$\tilde{\mathbf{K}}_e^{uH} = \mathbf{K}_e^{uH} - \mathbf{K}_e^{uD}(\mathbf{K}_e^{DD})^{-1}\mathbf{K}_e^{DH}\,, \tag{F.2}$$

$$\tilde{\mathbf{K}}_e^{Hu} = \mathbf{K}_e^{Hu} - \mathbf{K}_e^{HD}(\mathbf{K}_e^{DD})^{-1}\mathbf{K}_e^{Du}\,, \tag{F.3}$$

$$\tilde{\mathbf{K}}_e^{u\phi} = -\mathbf{K}_e^{uD}(\mathbf{K}_e^{DD})^{-1}\mathbf{K}_e^{D\phi}\,, \tag{F.4}$$

$$\tilde{\mathbf{K}}_e^{\phi u} = -\mathbf{K}_e^{\phi D}(\mathbf{K}_e^{DD})^{-1}\mathbf{K}_e^{Du}\,, \tag{F.5}$$

$$\tilde{\mathbf{K}}_e^{HH} = \mathbf{K}_e^{HH} - \mathbf{K}_e^{HD}(\mathbf{K}_e^{DD})^{-1}\mathbf{K}_e^{DH}\,, \tag{F.6}$$

$$\tilde{\mathbf{K}}_e^{H\phi} = -\mathbf{K}_e^{HD}(\mathbf{K}_e^{DD})^{-1}\mathbf{K}_e^{D\phi}\,, \tag{F.7}$$

$$\tilde{\mathbf{K}}_e^{\phi H} = -\mathbf{K}_e^{\phi D}(\mathbf{K}_e^{DD})^{-1}\mathbf{K}_e^{DH}\,, \tag{F.8}$$

and $$\tilde{\mathbf{K}}_e^{\phi\phi} = -\mathbf{K}_e^{\phi D}(\mathbf{K}_e^{DD})^{-1}\mathbf{K}_e^{D\phi}\,. \tag{F.9}$$

The components of the reduced vector of internal forces are

$$\tilde{\mathbf{F}}_e^{u} = \mathbf{F}_e^{u} - \mathbf{K}_e^{uD}(\mathbf{K}_e^{DD})^{-1}\mathbf{F}_e^{D}\,, \tag{F.10}$$

$$\tilde{\mathbf{F}}_e^{H} = \mathbf{F}_e^{H} - \mathbf{K}_e^{HD}(\mathbf{K}_e^{DD})^{-1}\mathbf{F}_e^{D}\,, \tag{F.11}$$

and $$\tilde{\mathbf{F}}_e^{\phi} = \mathbf{F}_e^{\phi} - \mathbf{K}_e^{\phi D}(\mathbf{K}_e^{DD})^{-1}\mathbf{F}_e^{D}\,. \tag{F.12}$$

References

Abdollahi, A., Peco, C., Millan, D., Arroyo, M., Arias, I., 2014. Computational evaluation of the flexoelectric effect in dielectric solids. J. Appl. Phys. 116 (9), 093502.

Amanatidou, E., Aravas, N., 2002. Mixed finite element formulations of strain-gradient elasticity problems. Comput. Methods Appl. Mech. Engrg. 191 (15–16), 1723–1751.

Argyris, J.H., Fried, I., Scharpf, D.W., 1968. The TUBA family of plate elements for the matrix displacement method. Aeronaut. J. 72 (692), 701–709.

Balcells-Quintana, O., Codony, D., Fernández-Méndez, S., 2022. C0-IPM with generalised periodicity and application to flexoelectricity-based 2D metamaterials. J. Sci. Comput. 92 (5), 1–29.

Bassiouny, E., Ghaleb, A.F., Maugin, G.A., 1988. Thermodynamical formulation for coupled electromechanical hysteresis effects—I, basic equations. Int. J. Eng. Sci. 26 (12), 1279–1295.

Bassiouny, E., Maugin, G.A., 1989. Thermodynamical formulation for coupled electromechanical hysteresis effects—IV. Combined electromechanical loading. Internat. J. Engrg. Sci. 27 (8), 989–1000.

Biot, M.A., 1965. Mechanics of Incremental Deformations. Wiley, New York.

Bursian, E.V., Zaikovskii, O.I., Makarov, K.V., 1969. Ferroelectric plate polarization by bending. Izv. Akad. Nauk SSSR Ser. Fiz. 33 (7), 1098.

Cao, Y., Li, Q., Chen, L.Q., Kalinin, S.V., 2015. Coupling of electrical and mechanical switching in nanoscale ferroelectrics. Appl. Phys. Lett. 107 (20), 202905.

Cao, H.X., Lo, V.C., Li, Z.Y., 2006. Simulation of flexoelectricity effect on imprint behavior of ferroelectric thin films. Solid State Commun. 138 (8), 404–408.

Cao, Y., Morozovska, A., Kalinin, S.V., 2017. Pressure-induced switching in ferroelectrics: Phase-field modeling, electrochemistry, flexoelectric effect, and bulk vacancy dynamics. Phys. Rev. B 96 (18), 184109.

Chaplya, P.M., Carman, G.P., 2001. Dielectric and piezoelectric response of lead zirconate–lead titanate at high electric and mechanical loads in terms of non-180 domain wall motion. J. Appl. Phys. 90 (10), 5278–5286.

Chen, H.T., Soh, A.K., Ni, Y., 2014. Phase field modeling of flexoelectric effects in ferroelectric epitaxial thin films. Acta Mech. 225 (4–5), 1323–1333.

Codony, D., Gupta, P., Marco, O., Arias, I., 2021a. Modeling flexoelectricity in soft dielectrics at finite deformation. J. Mech. Phys. Solids Eng. 146, 104182.

Codony, D., Marco, O., Fernández-Méndez, S., Arias, I., 2019. An immersed boundary hierarchical B-spline method for flexoelectricity. Comput. Methods Appl. Mech. Engrg. 354, 750–782.

Codony, D., Mocci, A., Barceló-Mercader, J., Arias, I., 2021b. Mathematical and computational modeling of flexoelectricity. J. Appl. Phys. 130, 231102.

Cross, L.E., 2006. Flexoelectric effects: Charge separation in insulating solids subjected to elastic strain gradients. J. Mater. Sci. 41, 53–63.

Dasgupta, S., Sengupta, D., 1990. A higher-order triangular plate bending element revisited. Internat. J. Numer. Methods Engrg. 30 (3), 419–430.

Deng, F., Deng, Q., Yu, W., Shen, S., 2017. Mixed finite elements for flexoelectric solids. J. Appl. Mech. 84 (8), 081004.

Deng, F., Yu, W., Liang, X., Shen, S., 2023. A mixed finite element method for large deformation of flexoelectric materials. Appl. Math. Model. 118, 303–321.

Ghasemi, H., Park, H.S., Rabczuk, T., 2017. A level-set based IGA formulation for topology optimization of flexoelectric materials. Comput. Methods Appl. Mech. Engrg. 313, 239–258.

Gil, A.J., Ortigosa, R., 2016. A new framework for large strain electromechanics based on convex multi-variable strain energies: Variational formulation and material characterisation. Comput. Methods Appl. Mech. Engrg. 302, 293–328.

Gruverman, A., Rodriguez, B.J., Kingon, A.I., Nemanich, R.J., Tagantsev, A.K., Cross, J.S., Tsukada, M., 2003. Mechanical stress effect on imprint behavior of integrated ferroelectric capacitors. Appl. Phys. Lett. 83 (4), 728–730.

Gu, Y., Hong, Z., Britson, J., Chen, L.Q., 2015. Nanoscale mechanical switching of ferroelectric polarization via flexoelectricity. Appl. Phys. Lett. 106 (2), 022904.

Gusev, A.A., Lurie, S.A., 2017. Symmetry conditions in strain gradient elasticity. Math. Mech. Solids 22 (4), 683–691.

Halphen, B., Nguyen, Q.S., 1975. Sur les matéraux standards généralisés. J. Mec. 14 (1), 39–63.

Jaffe, B., Cook, W.R., Jaffe, H., 1971. Piezoelectric Ceramics. Academic Press, London, New York.

Jiang, L., Tang, J., Zhou, Y., Yang, Q., Zhang, Y., Guo, L., Zhong, X., 2015a. Simulations of local-mechanical-stress-induced ferroelectric polarization switching by a multi-field coupling model of flexoelectric effect. Comput. Mater. Sci. 108, 309–315.

Jiang, L., Zhou, Y., Zhang, Y., Yang, Q., Gu, Y., Chen, L.Q., 2015b. Polarization switching of the incommensurate phases induced by flexoelectric coupling in ferroelectric thin films. Acta Mater. 90, 344–354.

Kamlah, M., 2001. Ferroelectric and ferroelastic piezoceramics - modeling of electromechanical hysteresis phenomena. Contin. Mech. Thermodyn. 4 (13), 219–268.

Kamlah, M., Böhle, U., 2001. Finite element analysis of piezoceramic components taking into account ferroelectric hysteresis behavior. Int. J. Solids Struct. 38 (4), 605–633.

Kamlah, M., Jiang, Q., 1999. A constitutive model for ferroelectric PZT ceramics under uniaxial loading. Smart Mater. Struct. 8 (4), 441–459.

Kamlah, M., Wang, Z., 2003. A thermodynamically and microscopically motivated constitutive model for piezoceramics. Comput. Mater. Sci. 28 (3–4), 409–418.

Landis, C.M., 2002. Fully coupled, multi-axial, symmetric constitutive laws for polycrystalline ferroelectric ceramics. J. Mech. Phys. Solids 50 (1), 127–152.

Landis, C.M., 2004. Non-linear constitutive modeling of ferroelectrics. Curr. Opin. Solid State Mater. Sci. 8 (1), 59–69.

Liu, C., Wang, J., Xu, G., Kamlah, M., Zhang, T.Y., 2019. An isogeometric approach to flexoelectric effect in ferroelectric materials. Int. J. Solids Struct. 162, 198–210.

Lu, H., Bark, C.W., Esque De Los Ojos, D., Alcala, J., Eom, C.B., Catalan, G., Gruverman, A., 2012. Mechanical writing of ferroelectric polarization. Science 336 (6077), 59–61.

Ma, W., Cross, L.E., 2003. Strain-gradient-induced electric polarization in lead zirconate titanate ceramics. Appl. Phys. Lett. 82 (19), 3293–3295.

Ma, W., Cross, L.E., 2005. Flexoelectric effect in ceramic lead zirconate titanate. Appl. Phys. Lett. 86, 072905.

Ma, W., Cross, L.E., 2006. Flexoelectricity of barium titanate. Appl. Phys. Lett. 88, 232902.

Mao, S., Purohit, P.K., Aravas, N., 2016. Mixed finite-element formulations in piezoelectricity and flexoelectricity. Proc. R. Soc. A 472, 20150879.

2022. MATLAB, Version 9.12.0.1884302 (R2022a). The MathWorks Inc., Natick, Massachusetts.

Mehling, V., Tsakmakis, C., Gross, D., 2007. Phenomenological model for the macroscopical material behavior of ferroelectric ceramics. J. Mech. Phys. Solids 55 (10), 2106–2141.

Miehe, C., 2002. Strain-driven homogenization of inelastic microstructures and composites based on an incremental variational formulation. Internat. J. Numer. Methods Engrg. 55 (11), 1285–1322.

Miehe, C., Rosato, D., Kiefer, B., 2011. Variational principles in dissipative electro-magneto-mechanics: A framework for the macro-modeling of functional materials. Internat. J. Numer. Methods Engrg. 86 (10), 1225–1276.

Mindlin, R.D., Eshel, N., 1968. On first strain-gradient theories in linear elasticity. Int. J. Solids Struct. 4 (1), 109–124.

Moulson, A.J., Herbert, J.M., 2003. Electroceramics: Materials, Properties, Applications. John Wiley & Sons, London, Chichester.
Nguyen, B.H., Zhuang, X., Rabczuk, T., 2018. Numerical model for the characterization of Maxwell-Wagner relaxation in piezoelectric and flexoelectric composite material. Comput. Struct. 208, 75–91.
Nguyen, B.H., Zhuang, X., Rabczuk, T., 2019. NURBS-based formulation for nonlinear electro-gradient elasticity in semiconductors. Comput. Methods Appl. Mech. Engrg. 346, 1074–1095.
Ortiz, M., Simo, J.C., 1986. An analysis of a new class of integration algorithms for elastoplastic constitutive relations. Internat. J. Numer. Methods Engrg. 23 (3), 353–366.
Ortiz, M., Stainier, L., 1999. The variational formulation of viscoplastic constitutive updates. Comput. Methods Appl. Mech. Engrg. 171 (3–4), 419–444.
Petera, J., Pittman, J.F.T., 1994. Isoparametric hermite elements. Internat. J. Numer. Methods Engrg. 37 (20), 3489–3519.
Polizzotto, C., 2016. A note on the higher order strain and stress tensors within deformation gradient elasticity theories: Physical interpretations and comparisons. Int. J. Solids Struct. 90, 116–121.
Radovitzky, R., Ortiz, M., 1999. Error estimation and adaptive meshing in strongly nonlinear dynamic problems. Comput. Methods Appl. Mech. Engrg. 172 (1–4), 203–240.
Roy, P., Roy, D., 2019. Peridynamics model for flexoelectricity and damage. Appl. Math. Model. 68, 82–112.
Serrao, P.H., Kozinov, S., 2023. Robust mixed FE for analyses of higher-order electromechanical coupling in piezoelectric solids. Comput. Mech. 1–15.
Serrao, P.H., Kozinov, S., 2024. Numerical modeling of ferroelectric materials in the presence of flexoelectricity. Comput. Methods Appl. Mech. Engrg. 424, 116888.
Shu, J.Y., King, W.E., Fleck, N.A., 1999. Finite elements for materials with strain gradient effects. Internat. J. Numer. Methods Engrg. 44 (3), 373–391.
Shu, L., Liang, R., Rao, Z., Fei, L., Ke, S., Wang, Y., 2019. Flexoelectric materials and their related applications: A focused review. J. Adv. Ceram. 8, 153–173.
Simo, J.C., Honein, T., 1990. Variational formulation, discrete conservation laws, and path-domain independent integrals for elasto-viscoplasticity. J. Appl. Mech. 57 (3), 488–497.
Sladek, J., Sladek, V., Tian, X., Deng, Q., 2022. Mixed FEM for flexoelectric effect analyses in a viscoelastic material. Int. J. Solids Struct. 234, 111269.
Sutter, F., 2024. Materiell Nichtlineare Kontinuumsmodellierung Ferroelektrischer Funktionskeramiken Mit Piezoelektrischen Und Flexoelektrischen Eigenschaften. KIT Scientific Publishing, Karlsruhe.
Sutter, F., Kamlah, M., 2023. Variational free energy based macroscopical modeling of ferroelectroelasticity. J. Mech. Phys. Solids 178, 105341.
Tannhäuser, K., Serrao, P.H., Kozinov, S., 2023. Second-order collocation-based mixed FEM for flexoelectric solids. Solids 4, 39–70.
Tannhäuser, K., Serrao, P.H., Kozinov, S., 2024. A three-dimensional collocation finite element method for higher-order electromechanical coupling. Comput. Struct. 291, 107219.
Thai, T.Q., Rabczuk, T., Zhuang, X., 2018. A large deformation isogeometric approach for flexoelectricity and soft materials. Comput. Methods Appl. Mech. Engrg. 341, 718–739.
Tian, X., Sladek, J., Sladek, V., Deng, Q., Li, Q., 2021. A collocation mixed finite element method for the analysis of flexoelectric solids. Int. J. Solids Struct. 271–218, 27–39.
Ventura, J., Codony, D., Fernández-Méndez, S., 2021. A C0 interior penalty finite element method for flexoelectricity. J. Sci. Comput. 88, 1–24.
Wang, B., Gu, Y., Zhang, S., Chen, L.Q., 2019. Flexoelectricity in solids: Progress, challenges, and perspectives. Prog. Mater. Sci. 106, 100570.
Wang, Z., Zhang, X.X., Wang, X., Yue, W., Li, J., Miao, J., Zhu, W., 2013. Giant flexoelectric polarization in a micromachined ferroelectric diaphragm. Adv. Funct. Mater. 23 (1), 124–132.
Wilkins, M.L., 1964. Calculation of elastic plastic flow. In: Alder, B., Fernbach, S., Rotenberg, M. (Eds.), Methods in Computational Physics. Vol. 3, Academic Press, New York, pp. 271–277.
Witt, C., Kaiser, T., Menzel, A., 2023. Modelling and numerical simulation of remodelling processes in cortical bone: An IGA approach to flexoelectricity-induced osteocyte apoptosis and subsequent bone cell diffusion. J. Mech. Phys. Solids Eng. 173, 105194.
Witt, C., Kaiser, T., Menzel, A., 2024. An IGA-FEA model for flexoelectricity-induced healing of microcracks in cortical bone. Comput. Methods Appl. Mech. Engrg. 425, 116919.
Wriggers, P., 2008. Nonlinear Finite Element Methods. Springer-Verlag, Berlin, Heidelberg.
Yudin, P.V., Tagantsev, A.K., 2013. Fundamentals of flexoelectricity in solids. Nanotechnology 24, 432001.
Yvonnet, J., Nguyen, L.P., 2017. A numerical framework for modeling flexoelectricity and Maxwell stress in soft dielectrics at finite strains. Comput. Methods Appl. Mech. Engrg. 313, 450–482.
Zhuang, X., Nanthakumar, S.S., Rabczuk, T., 2020a. A meshfree formulation for large deformation analysis of flexoelectric structures accounting for the surface effects. Eng. Anal. Bound. Elem. 120, 153–165.
Zhuang, X., Nguyen, B.H., Nanthakumar, S.S., Tran, T.Q., Alajlan, N., Rabczuk, T., 2020b. Computational modeling of flexoelectricity — A review. Energies 13 (6), 1326.
Zienkiewicz, O.C., Taylor, R.L., Zhu, J.Z., 2005. The Finite Element Method: Its Basis and Fundamentals, sixth ed. Elsevier Butterworth-Heinemann, Oxford.
Zubko, P., Catalan, G., Buckley, A., Welche, P.R.L., Scott, J.F., 2007. Strain-gradient-induced polarization in SrTiO 3 single crystals. Phys. Rev. Lett. 99 (16), 167601.
Zubko, P., Catalan, G., Tagantsev, A.K., 2013. Flexoelectric effect in solids. Annu. Rev. Mater. Res. 43, 387–421.
Zybell, L., Mühlich, U., Kuna, M., Zhang, Z.L., 2012. A three-dimensional finite element for gradient elasticity based on a mixed-type formulation. Comput. Mater. Sci. 52 (1), 268–273.